

Twentieth century ENSO-related precipitation mean states in twentieth century reanalysis, reconstructed precipitation and CMIP5 models

Ni Dai^{1,3}  · Phillip A. Arkin²

Received: 12 November 2015 / Accepted: 19 June 2016 / Published online: 8 July 2016
© Springer-Verlag Berlin Heidelberg 2016

Abstract El Niño–Southern Oscillation (ENSO)-related precipitation during the entire twentieth century is compared among the twentieth century reanalysis (20CR), a statistically reconstructed precipitation dataset (REC) and 30 Coupled Model Intercomparison Project Phase 5 (CMIP5) models. Empirical orthogonal functions, ENSO-related precipitation composites based on sea surface temperature (SST)-constructed ENSO index and singular value decomposition (SVD) are employed to extract ENSO-related precipitation/SST signals in each dataset. With the background trend being removed in all of the data, our results show that the REC and the 20CR resemble both in their precipitation climatology and ENSO-related precipitation results. The biases in the CMIP5 models precipitation climatology such as dry equator over the Pacific Ocean, “double-intertropical convergence zones (ITCZs)” and overly zonal Southern Pacific convergence zone (SPCZ) are major reasons for lowering spatial correlations with the REC and the 20CR precipitation climatology. Two groups of CMIP5 models are built based on severity of these biases in their precipitation background and the spatial correlations of ENSO-related precipitation with the observations. Compared with the group with more severe biases in its precipitation climatology, the group with smaller

biases tends to produce more ENSO-like precipitation patterns, simulate more realistic mean magnitude and seasonal variability of ENSO precipitation signals, as well as generating better ENSO-related SST/precipitation correlation patterns produced in its SVD analysis. The ENSO-related precipitation biases in the CMIP5 models over the western Pacific and Indian Ocean, as well as the equatorial Pacific, are strongly related with their precipitation climatology biases over these regions. The ENSO-related precipitation biases over the off-equator eastern Pacific Ocean are associated with both the “double-ITCZs” biases in the precipitation climatology and the ENSO-related SST biases in the models.

Keywords ENSO · Precipitation · Twentieth century reanalysis · CMIP5 models · Spatial fields · Biases · Dry equator · Double-ITCZs

1 Introduction

The El Niño–Southern Oscillation (ENSO) phenomenon is the most significant example of interannual atmosphere–ocean coupling in the global climate system (McPhaden et al. 2006). It is associated with changes in surface easterly winds in the tropics, especially over the Pacific Ocean, resulting in thermocline as well as sea surface temperature (SST) changes in both amplitude and distribution. With the wind stress and SST variations, the strength and location of atmospheric convection and the Walker circulation also change (Lindzen and Nigam 1987), leading to different precipitation patterns over the tropical Pacific Ocean (e.g. Wang et al. 2004; McPhaden et al. 2006), and greatly affecting a number of populated regions such as the Maritime Continent (Philander 1985), and the South and North

✉ Ni Dai
ndai@umd.edu

¹ Department of Atmospheric and Oceanic Science, University of Maryland, College Park, MD, USA

² Earth System Science Interdisciplinary Center, University of Maryland, College Park, MD, USA

³ Cooperative Institute for Climate and Satellites – Maryland, Earth System Science Interdisciplinary Center, University of Maryland, College Park, MD, USA

American west coasts (Ropelewski and Halpert 1987). As ENSO is one of the better observed and understood climate phenomena (e.g. Clarke 2008) and precipitation is one of the most difficult parameters to simulate in global climate models (Räisänen 2007), the validation of ENSO-related precipitation in coupled ocean–atmosphere climate models is vital in order to understand the phenomenon and to build confidence for the models (Guilyardi et al. 2009), as well as to better predict ENSO-related precipitation.

Over the last two decades, coupled global climate models (GCMs) have been improved significantly (Reichler and Kim 2008). The Coupled Model Intercomparison Project Phase 5 (CMIP5) (Taylor et al. 2012) collects most of the current state-of-the-art GCMs and provides excellent opportunities to compare inter-model diversity of ENSO-related precipitation variability and to further understand ENSO. Previous studies suggest that CMIP5 models have the ability to simulate ENSO, including its teleconnections, more realistically than their precursors (e.g. Bellenger et al. 2014; Kim et al. 2014; Ham and Kug 2015). However, there still exist biases of ENSO-related precipitation in the models. One of the major biases is that the center of the positive precipitation anomalies is located about 20° west of the observed one, which is consistent with the westward extended ENSO SST anomalies and ENSO zonal winds (Zhang and Sun 2014; Ham and Kug 2015). Also, the meridional width of the positive precipitation anomalies is usually narrower in the models than the observed one, which is due to the narrow sea surface temperature anomalies (SSTA) (Zhang and Jin 2012). These biases additionally lead to systematic errors in the lifecycles and variations of ENSO-related precipitation in the models (Brown et al. 2014). Previous studies suggest that the model biases in subsurface thermocline, SST, sea level pressure (SLP) and the resulting Hadley and Walker cells all play parts in the biases of the location and amplitude of ENSO and ENSO-related precipitation in the global circulation models (Kirtman et al. 2002; Zhang and Jin 2012; Ham and Kug 2014).

Besides the biases mentioned above, the mean state of precipitation in the models might also contribute to the spatial biases of the ENSO-related precipitation (Watanabe et al. 2010; Brown et al. 2013a; Ham and Kug 2014). One of the most well known biases of the precipitation climatology in models is the double intertropical convergence zones (ITCZs) pattern, that is, simulated precipitation tends to be underestimated over the equator but overestimated both north and south of the equator in the eastern Pacific during most of the year (Mechoso et al. 1995; Zhang 2001; Lin 2007; Bellucci et al. 2010; Brown et al. 2013a). The “double-ITCZs” bias is usually caused by (1) model biases of the large-scale circulations such as too strong and narrow and westward extended equatorial cold tongue in the eastern equatorial Pacific associated with strong easterlies,

generating unrealistic convergence over the north and south edges of the cold tongue (Mechoso et al. 1995; Wittenberg et al. 2006; Lin 2007); (2) model biases of the regional scale circulations such as the underestimated cross-equatorial winds over the southeastern Pacific leading to less upwelling in this region and thus positive SST biases (Mechoso et al. 1995; de Szoeke and Xie 2008); (3) biases of the variables in the convective processes such as SST gradient (e.g. Lindzen and Nigam 1987), surface heat fluxes, or thresholds for deep convection (Bellucci et al. 2010); (4) parameterization biases and oversensitivity in ocean–atmosphere feedbacks and cloud schemes (Chikira and Sugiyama 2010; Hirota and Takayabu 2013). In CMIP5, more models show the “double-ITCZs” problem than their CMIP3 precursors (Grose et al. 2014). Hwang et al. (2013) points out that the CMIP5 models with more energy flux into the Southern Hemisphere atmosphere tend to have stronger “double-ITCZs” bias. Another well-known bias in the models is the “dry equator” over the Pacific Ocean which is usually caused by an overly narrow and strong cold tongue combined with excessively strong trade winds (Zhang and Jin 2012; Grose et al. 2014), as well as too far west warm pool eastern edge (Brown et al. 2014; Grose et al. 2014). The South Pacific convergence zone (SPCZ) is another feature that is difficult for models to simulate well. Similar to the ITCZ, the SPCZ is a band of precipitation formed by low-level wind convergence, located over the western and central South Pacific (e.g. Trenberth 1976; Vincent 1994). The SPCZs in the CMIP5 models are overly zonal and too far north and east in December–February in some models, without significant improvement from the precursor models in CMIP3 (Brown et al. 2013b; Grose et al. 2014). Brown et al. (2013b) points out that the SPCZ orientation bias in the CMIP5 models might be related to the absence of ocean heat flux-adjustment. Additionally, the “double-ITCZs”, dry equator and the SPCZ biases in the model precipitation mean state might not only have impacts on the ENSO-related precipitation, but also can be affected by the changes in the air–sea interaction during ENSO (Watanabe et al. 2010; Sun et al. 2014).

To reduce these biases of ENSO-related precipitation mean state and associated precipitation climatology ones in current GCMs, it is very important to validate the models with more observation datasets especially those covering a long time period (Räisänen 2007). Longer-term datasets contain more ENSO events than the shorter ones. Since each ENSO event is different from others, larger sample of ENSO events tends to produce more reliable typical ENSO mean states for both observations and model outputs. Especially in recent decades, as the “warm pool” El Niño events occur more frequently (Kug et al. 2009; Yeh et al. 2014) and the CMIP5 models perform very diversely in simulating the two types of El Niño (“warm pool” and “cold

tongue”, Larkin and Harrison 2005; Kug et al. 2009), comparing the models with longer-term observations instead of datasets that only cover the most recent years would reduce more sampling biases in the characterization of typical ENSO mean states. In the past 2–3 years, better precipitation datasets that cover the whole twentieth century have become available, such as the twentieth century reanalysis (20CR) from NOAA (Compo et al. 2011) and statistically reconstructed precipitation (Smith et al. 2012). Thus, it is very useful to compare the CMIP5 models with these datasets along with century-long SST reanalyses over the twentieth century time span to further improve the understanding of the precipitation climatology and ENSO-related precipitation in these models. In this paper, we present spatial similarities and dissimilarities of the precipitation climatology and ENSO-related precipitation between the CMIP5 models and these newly developed datasets during the twentieth century, in order to identify the features that need to be improved in the models. We also show the spatial influences of the precipitation climatology on the ENSO-related precipitation in each dataset in order to explain some of these spatial dissimilarities.

This paper is organized as follows. Section 2 introduces the data and the methodology used. Sections 3 and 4 describe the characteristics of the precipitation climatology and mean state of ENSO-related precipitation in the reconstructed precipitation (REC), the 20CR and 30 CMIP5 models. In Sect. 3, the annually and seasonally averaged precipitation climatology in both observations and CMIP5 models is presented in order to compare the mean state of precipitation among the several datasets. In Sect. 4 we describe empirical orthogonal function (EOF) analysis of annually and seasonally-averaged ENSO precipitation anomalies to provide a general idea of the appearance of the mean ENSO-related precipitation in the whole twentieth century, and to evaluate how well the CMIP5 models reproduce these precipitation anomaly patterns. Section 5 further examines the spatial dissimilarities between the CMIP5 models and the other two datasets, and compares ENSO-related precipitation signals among these datasets. Section 6 further discusses some connections of the ENSO-related precipitation biases in the models with the precipitation climatology and ENSO-related SST biases and summarizes the major findings in this paper.

2 Datasets and methods

We chose 30 CMIP5 models (as detailed in Table 1) (Taylor et al. 2012) from ‘historical experiments’, which are carried out with all forcings including changes of atmospheric composition due to anthropogenic and volcanic influences, solar radiation, aerosol emissions and land use change.

These 30 models all have the same pre-industrial initial conditions in 1850 and are carried out to 2005. We examine 2 model output variables in this paper: precipitation (mm/day) and sea surface temperature (°C). All data are monthly averaged and have been interpolated to 2.5° by 2.5° grids.

For precipitation, we use the reconstructed precipitation analyses (REC) developed by NOAA/CICS (Smith et al. 2012) as the primary observational dataset. This dataset uses the global precipitation climatology project (GPCP V2, Adler et al. 2003; Huffman et al. 2009) as climatology, and is created by reconstructing spatial covariance modes of gauge data (global historical climatology network, GPCN) on land, using different mode weights. Over ocean, the precipitation data is reconstructed using statistics from modern (well-sampled) analyses with additional guidance from observed covariance of sea level pressure, SST (ERSST v3, Smith et al. 2008) and GPCP. The REC dataset contains monthly precipitation rate anomalies (mm/mon; converted to mm/day in our study), with a spatial resolution of 2.5° by 2.5°. Since this dataset has fewer observations at high latitudes, the domain of 75°S to 75°N is chosen for REC and all the other datasets. We also use the monthly twentieth century reanalysis (20CR) precipitation (Compo et al. 2011) as quasi-observational data. 20CR utilizes an NCEP atmosphere–land model with an Ensemble Kalman Filter data assimilation system (Whitaker and Hamill 2002) and assimilating only surface pressure and observed SLP to generate first-guess precipitation fields from 1871 to the present. The monthly Hadley Centre Sea Ice and SST dataset (HadISST, Rayner et al. 2003) provides the prescribed boundary condition. No observed precipitation is further assimilated to the 20CR. Thus, the 20CR precipitation is generated based on model parameterization and is substantially different from the observationally based REC precipitation. We interpolate 20CR precipitation into the same 2.5° by 2.5° resolution. For SST observations, we employ the ERSST v3/HadISST for analyses using REC/20CR precipitation respectively.

All data in our study are either annually or seasonally (e.g. December–January–February and June–July–August) averaged anomalies. The period used is from 1901 to 2005, and anomalies are calculated relative to the entire period. To clarify the ENSO signals in both the precipitation and SST datasets, we applied a 15-year high pass filter prior to other calculations to remove lower frequency variations such as the background trend of the century, in order to permit relatively impartial spatial and temporal comparisons among all the data. The 15-year high pass filter lets both the classic ENSO variability (period of 2–7 years) and some of ENSO decadal signals pass through.

Two methods are used to extract ENSO signals in all datasets. The first is empirical orthogonal function (EOF) analysis, which was used with both the annually and

Table 1 List of the 30 CMIP5 models used in this study

Model center or group	Institute ID	CMIP5 models	Runs
Canadian Centre for Climate Modelling and Analysis	CCCma	CanESM2	5
Centro Euro-Mediterraneo per I Cambiamenti Climatici	CMCC	CMCC-CM	1
		CMCC-CMS	1
Centre National de Recherches Meteorologiques/Centre Europeen de Recherche et Formation Avancees en Calcul Scientifique	CNRM-CERFACS	CNRM-CM5	10
CSIRO (Commonwealth Scientific and Industrial Research Organisation, Australia), and BOM (Bureau of Meteorology, Australia)	CSIRO-BOM	ACCESS1.0	1
		ACCESS1.3	1
Commonwealth Scientific and Industrial Research Organisation in collaboration with the Queensland Climate Change Centre of Excellence	CSIRO-QCCCE	CSIRO-Mk3.6.0	10
Institute for Numerical Mathematics	INM	INM-CM4	1
Institut Pierre-Simon Laplace	IPSL	IPSL-CM5A-LR	6
		IPSL-CM5A-MR	2
		IPSL-CM5B-LR	1
Atmosphere and Ocean Research Institute (The University of Tokyo), National Institute for Environmental Studies, and Japan Agency for Marine-Earth Science and Technology	MIROC	MIROC5	5
Met Office Hadley Centre (additional HadGEM2-ES realizations contributed by Instituto Nacional de Pesquisas Espaciais)	MOHC	HadCM3	10
Max Planck Institute for Meteorology (MPI-M)	MPI-M	MPI-ESM-LR	2
		MPI-ESM-P	3
Meteorological Research Institute	MRI	MRI-CGCM3	3
NASA Goddard Institute for Space Studies	NASA-GISS	GISS-E2-H	4
		GISS-E2-H-CC	1
		GISS-E2-R	5
		GISS-E2-R-CC	1
National Center for Atmospheric Research	NCAR	CCSM4	5
Norwegian Climate Centre	NCC	NorESM1-M	3
		NorESM1-ME	1
National Institute of Meteorological Research/Korea Meteorological Administration	NIMR/KMA	HadGEM2-AO	1
		Geophysical Fluid Dynamics Laboratory	NOAA-GFDL
		GFDL-ESM2G	1
		GFDL-ESM2M	1
		National Science Foundation, Department of Energy, National Center for Atmospheric Research	NSF-DOE-NCAR
		CESM1-CAM5	3
		CESM1-FASTCHEM	3

seasonally averaged data. With the seasonal cycle and background trend removed, the first few EOF modes can be expected to show the major ENSO signals (e.g. Dai and Wigley 2000).

For the second method, we employ El Niño and La Niña composites in order to separate the El Niño- and the La Niña-related precipitation signals from the combined ENSO signals using the EOF methods. Since the Nino3.4 region might be inappropriate in models with SST and precipitation climatologies that differ from observed, we define an El Niño/La Niña index by using the first time series associated with SST EOF results. El Niño time periods, years or seasons in this paper, are those in the top quartile; La Niña years are those in the lowest quartile. We

average precipitation anomalies for all El Niño or La Niña time periods to calculate composite precipitation anomaly global maps. To quantitatively compare these composite results, we apply a method created by Curtis and Adler (2000) that generates an ENSO-related precipitation index. In their paper, they chose two gridded boxes (10°N–10°S, 90°–150°E and 10°N–10°S, 160°–100°W) to represent the Maritime Continent (MC) and central to eastern Pacific (P) separately. A 10° latitude × 50° longitude block was used to move inside of the two bigger boxes by 2.5° increments. The El Niño-related precipitation index (EI) is produced using the maximum of the averaged block in the P box minus the minimum of the averaged block in the MC box; La Niña-related precipitation index (LI) is created from the

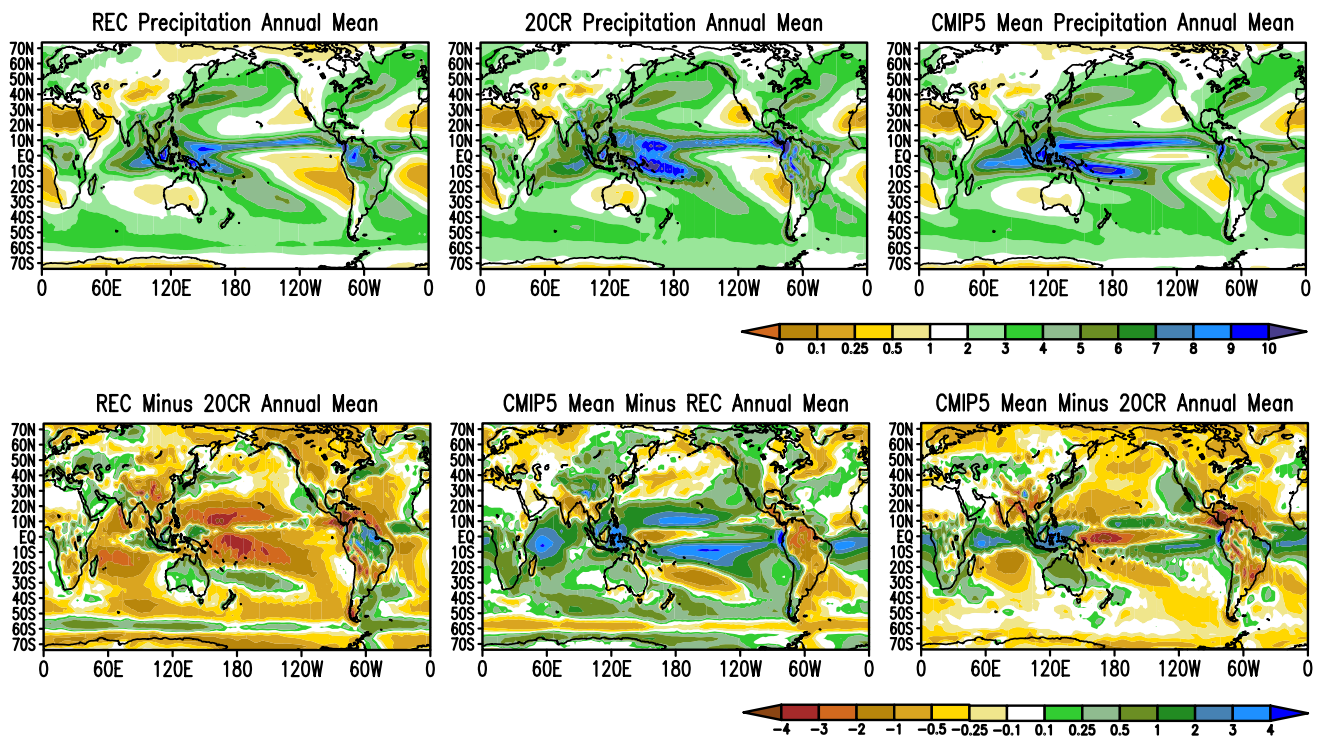


Fig. 1 Annual-averaged precipitation climatology of the REC, the 20CR and the mean of the 30 CMIP5 models (mm/day, 1901–2005) and the difference maps among them (the REC minus the 20CR, the

mean of the 30 CMIP5 models minus the REC and the mean of the 30 CMIP5 models minus the 20CR)

maximum of the averaged block in the MC box minus the minimum of the averaged block in the P box. EI minus LI generates the ENSO-related precipitation index.

3 Precipitation climatology

We present in Fig. 1 the annually averaged precipitation climatologies of the REC, the 20CR, the mean of the 30 CMIP5 models and the difference maps among them. The REC climatology resembles that of the 20CR, with the spatial correlation coefficient equal to 0.87. Seasonally averaged correlation coefficients between these two datasets are high as well, equaling to 0.84 (MAM), 0.87(JJA), 0.89(SON) and 0.89(DJF) separately.

We have also compared both of the REC and the 20CR with satellite datasets TRMM 3B43 (Huffman et al. 2007) using the time span of 1998–2005. The averaged correlation coefficient of the REC (~0.95) is higher than the 20CR (~0.87). Overall, the REC is drier than the 20CR in general over the ocean by 0.50 mm/day (annual), 0.60 mm/day (JJA) and 0.46 mm/day (DJF). The spatial differences between the REC and the 20CR are the largest in the tropics where precipitation is the heaviest, especially the ITCZ region over the central to western part of Pacific Ocean and the SPCZ region. Figure 2 shows the seasonal cycle of the

zonal-averaged (150°E–90°W) meridional distribution of precipitation over the tropical Pacific and indicates that the differences above are consistent throughout the seasons. The two datasets also disagree over the easternmost Pacific Ocean at 10°N where the ITCZ in the REC is weaker than the 20CR one. The ocean regions where the REC is wetter than the 20CR are the southern edge of the Pacific ITCZ, western part of the Indo-Pacific warm pool, the eastern Atlantic ITCZ region, the southern edge of the SPCZ, the northern Pacific subtropics, and the storm tracks in both northern and southern hemisphere. Over land, the REC has more rainfall over tropical South America, Northern Australia, central Africa, Mediterranean region and Eastern Europe, while the 20CR is wetter over North America, the middle part of South America as well as the Indian monsoon region especially during JJA.

The spatial correlation coefficients between the 30 CMIP5 models and the two observations (Table 1) range from 0.59 to 0.87, with an average of 0.76. The annual-averaged coefficients are the highest (~0.79), and the ones during DJF (~0.77) and SON (~0.78) are higher than during JJA (~0.75) and MAM (~0.72). From the annual results (Fig. 1), the biggest disagreements of the CMIP5 models with the observations are that the models show the ‘double-ITCZs’ in the eastern tropical Pacific Ocean and the Atlantic Ocean, an overly zonal and eastward-extended SPCZ

and a westward-extended drier band over the equator that separate the SPCZ from the ITCZ. The seasonal results (Fig. 2) of the CMIP5 models show that the northern Pacific ITCZs and the averaged precipitation over southern tropical Pacific are stronger in most of the models than in the observations throughout the year, while the equators are consistently drier in many models. The seasonal precipitation climatology maps of the CMIP5 models (not shown) indicate that, unlike the observations that only exhibit “double-ITCZs” (DI) in MAM, most of the models have the DI pattern in other seasons, especially in DJF, which leaves the weakened but still obvious DI signals in their annual-averaged results. In DJF, the models’ SPCZs are the strongest and most tilted, however, most of the SPCZs have unrealistic eastward-extended zonal branches that reach to Peru. The largest difference of this “southern-ITCZ” in the eastern Pacific between the models and the observations are found in MAM, and for some models, the “southern-ITCZ” becomes so strong that its northern counterpart even disappears (e.g. MIROC5 and CCSM4). From MAM to JJA, the rainfall band jumps from the Southern Hemisphere to the Northern Hemisphere. The “northern-ITCZ” bias in models reaches its maximum in SON. Figure 2 and Table 1 indicate that models exhibiting the most severe “double-ITCZs” problems (e.g. GISS-E2-H and GISS-E2-H-CC) and the ones with wide and seasonally-consistent “dry equators” (e.g. CSIRO-Mk3-6-0 and MPI-ESM-P) are among those models that have lowest correlations with both observation datasets, while the models with very weak “double-ITCZs” or “dry equators” biases (e.g. CESM1-BGC and CCSM4) tend to correlate better with the observations.

In addition to the DI, SPCZ and dry equator problem, the models also exhibit common overestimated precipitation (Fig. 1) over the tropical Atlantic and Indian Ocean, Maritime Continent, northern Pacific subtropical high region, central and southern Africa and Australia, as well as

underestimated rainfall over northern extra-tropical storm track region, central America and tropical South America and central United States. The theories for the GCM-based overestimated precipitation over tropical Atlantic and Indian Ocean are similar to those of the Pacific DI patterns from previous studies: (1) the simulation of large-scale circulations is biased, resulting in unrealistic magnitude and location of regional convection and precipitation; (2) poor parameterizations and over-sensitivity of atmosphere–ocean coupling and feedbacks further affect the circulations (e.g. Bollasina et al. 2011). The underestimated rainfall over the land (e.g. tropical South America) is also related to model convective parameters and underestimated large-scale moisture convergence (Hwang et al. 2013).

4 Mean state of ENSO-related precipitation

4.1 Annually-averaged precipitation anomalies EOF results

4.1.1 REC and 20CR

In order to establish the mean state of ENSO-related precipitation for both observations and models, we first use EOF analysis on 15-year high-pass filtered annual-averaged precipitation anomalies. Figure 3 shows the first and second EOF modes of 20CR and REC annual-averaged precipitation anomalies. The time series of the first EOF modes (Fig. 3a) of the two observation datasets are strongly correlated with the Niño 3.4 Index ($r \sim 0.90$), and the spatial patterns are very similar to each other (pattern correlation coefficient $r \sim 0.89$) and to the precipitation anomalies patterns associated with ENSO in previous studies (e.g. Ropelewski and Halpert 1987; Xie and Arkin 1997; Dai and Wigley 2000). During its positive phase (El Niño), the

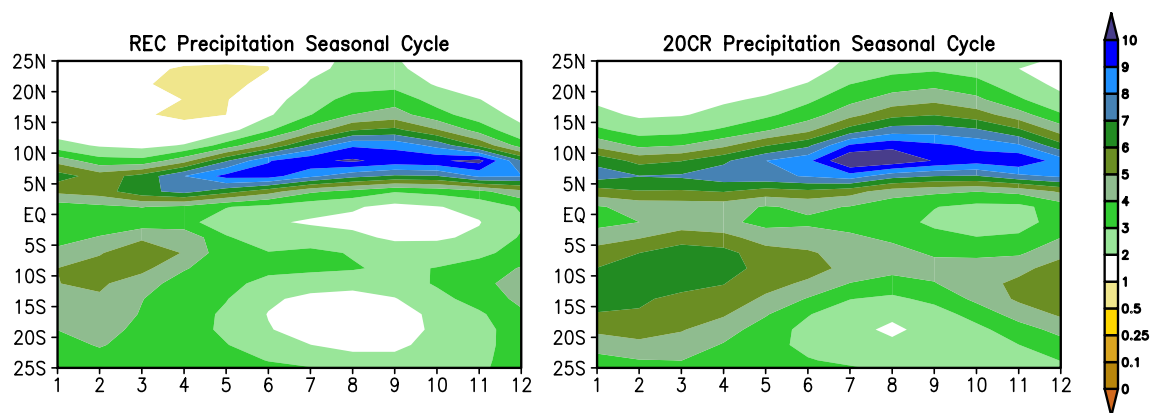


Fig. 2 Seasonal cycle of the meridional distribution of precipitation over the tropical Pacific Ocean (zonal average of 150°E–90°W) of the REC, the 20CR and the 30 CMIP5 models (mm/day, 1901–2005)

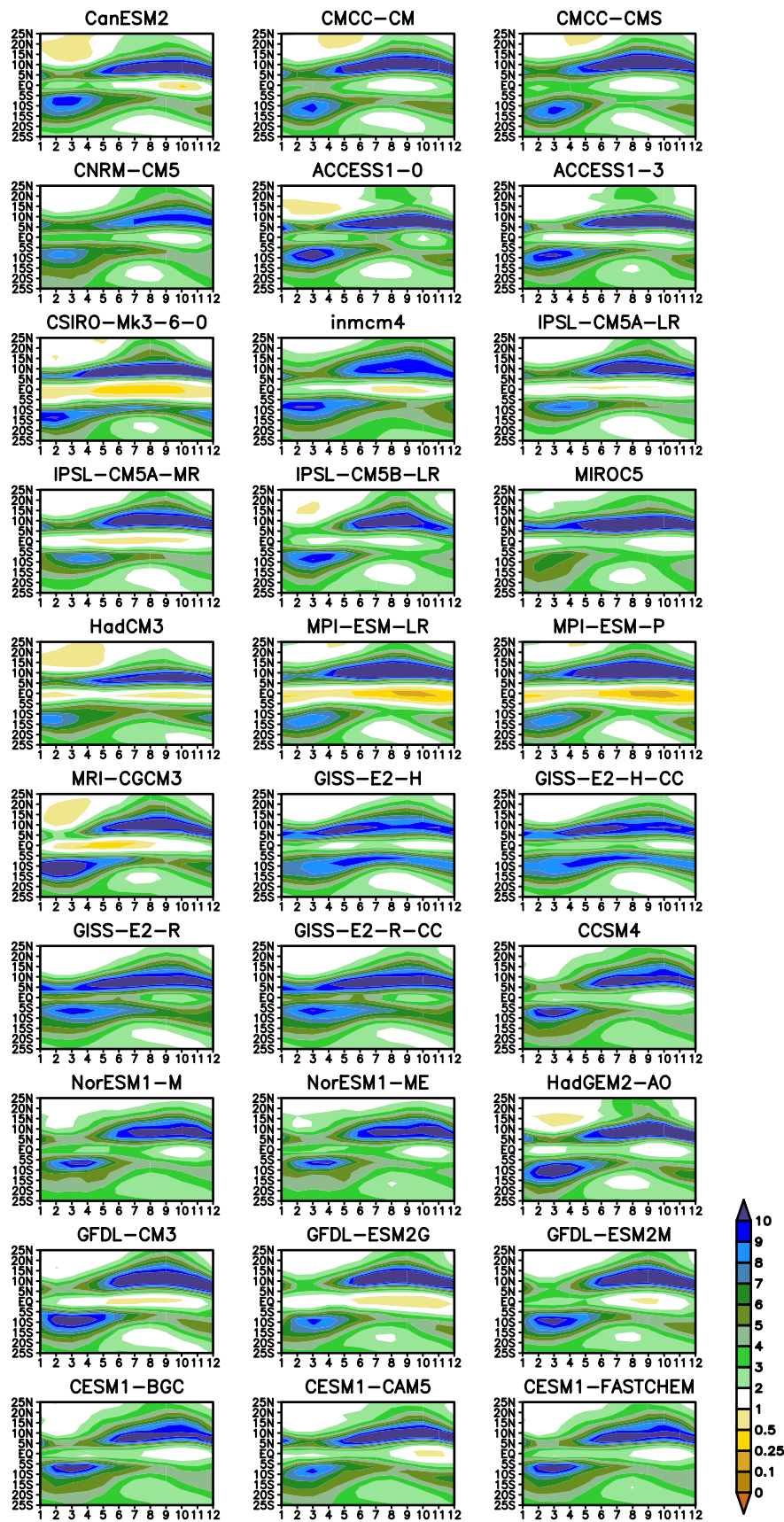


Fig. 2 continued

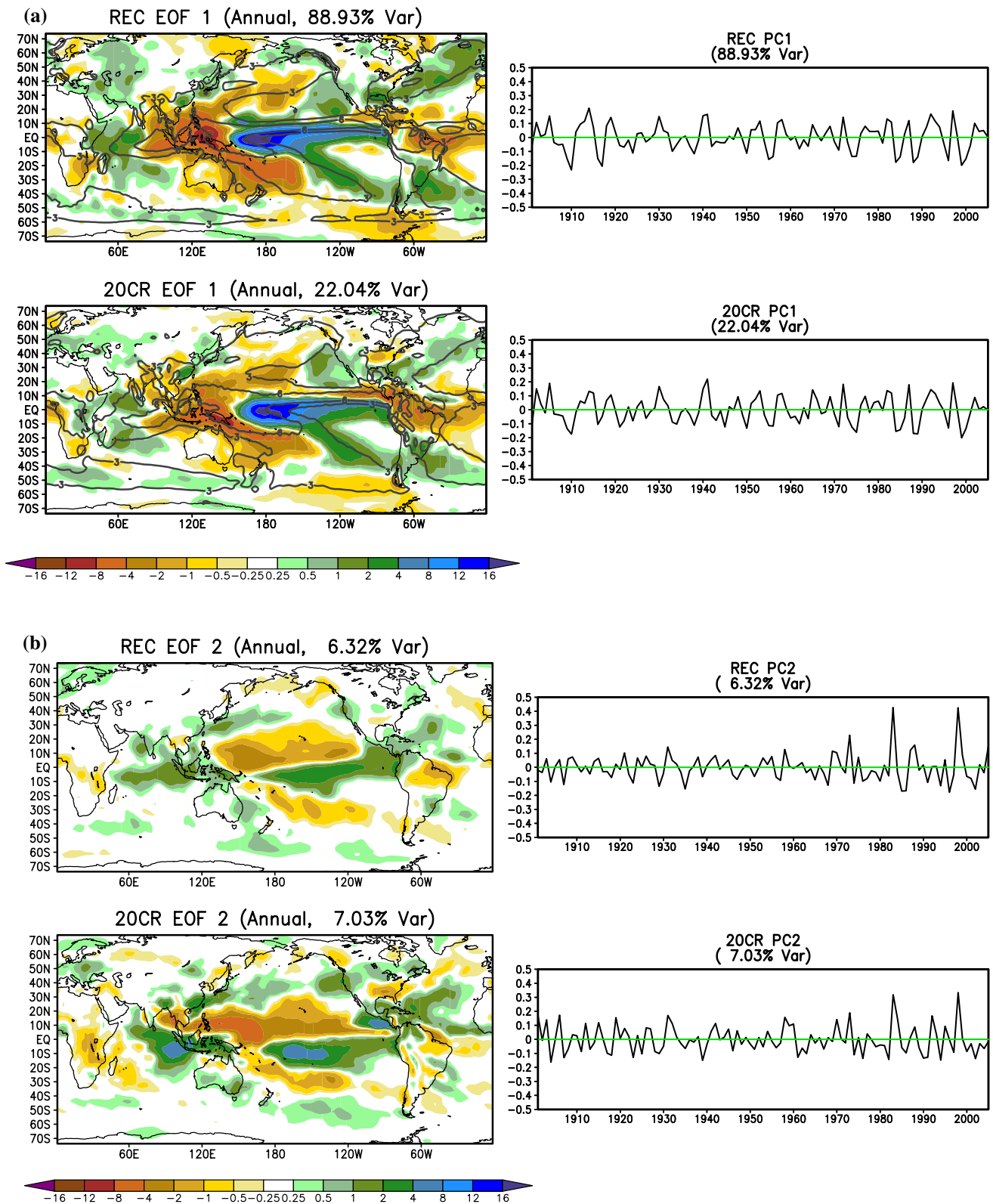


Fig. 3 First and second EOF results of the 2 observational annual-averaged precipitations anomalies (mm/day, 1901–2005) (*shading* is the precipitation anomalies EOF results; contours are the annual-

averaged precipitation climatology of 3 and 6 mm/day). **a** First EOF mode, **b** second EOF mode

SPCZ of the annual-averaged precipitation climatology (shown as the contours in Fig. 3a) moves northeastward and merges with the ITCZ leaving positive anomalies over the eastern and central Pacific Ocean (Vincent et al. 2011; Widlansky et al. 2012) as the shading maps show. Negative anomalies are over the Maritime Continent and spreading out poleward and eastward in a horseshoe pattern. The maximum positive anomalies in both the REC and the 20CR are located around 180°E. Although the spatial fields of the two observations strongly resemble each other, there are some differences in small spatial scale details. Overall, the REC precipitation anomaly map of the first EOF mode exhibits slightly greater contrast than does that of the 20CR, with larger positive anomalies over the central and northern Pacific Ocean, the Indian Ocean at 10°S, the northeastern Atlantic Ocean and Eastern Europe/western Asia, and larger negative anomalies over the Maritime Continent. In the eastern Pacific, the first 20CR mode is less symmetric about the equator, with negative anomalies over the “Northern-ITCZ” region and near neutral conditions over its counterpart in the Southern Hemisphere. Note that the first mode of the annual-averaged REC anomalies explains 85–89 % of the total variance, which is about 4–5 times larger than the 20CR. This is because that the annual first guess field of REC is generated by a limited number (approximately 10) of EOF modes of ERSST, the SLP field and the GPCP annual-average (Smith et al. 2012), which filters out finer spatial details included in the 20CR first mode. On average, the REC includes around 70 % of total explained variance of the 20CR.

The 2nd mode (Fig. 3b) spatial fields of both observations exhibit positive anomalies over the central and eastern tropical Pacific Ocean, Southeast Asia and the eastern part of the Indian Ocean. There are also some differences in detail between the REC and the 20CR spatial patterns. Positive precipitation anomalies in the 20CR are larger over the central Pacific Ocean, the north and tropical Atlantic Ocean, the eastern Indian Ocean, and Eastern Europe, while negative anomalies are larger in the western Pacific. Over the Eastern Pacific, the negative anomalies in the 20CR over the northern near-equatorial region, similar to those in the first mode, extend closer to the Central American coast than in the REC. This might suggest some background difference in precipitation anomalies over the eastern tropical Pacific Ocean between the dynamical 20CR model and the statistical REC model. The time series of both observation datasets show significantly larger positive anomalies in years 1973, 1983, and 1998. Those years are all the concluding years of strong El Niño episodes (1972–1973, 1982–1983 and 1997–1998, Wolter and Timlin 1998). In addition, when the 15-year high-pass filter is not applied, both observations exhibit an upward trend throughout the whole 105 years in the time series of the

2nd mode (not shown), with identical spatial fields as the detrended ones. These evidences suggest that the 2nd EOF mode is the residual of decadal to multi-decadal ENSO variability.

4.1.2 CMIP5 models

The spatial correlation coefficient (Table 3) average of the first EOF mode between the 30 CMIP5 models and the two observation datasets is about 0.58. The models that have relatively lower (higher) correlations with the observations in Table 2 also have similar performances in Table 3. Therefore, based on Tables 2 and 3, we pick 11 models from each half of these 30 CMIP5 models and build two groups. Group 1 is the “higher correlations” group, including the model CanESM2, CCSM4, CESM1-BGC, CESM1-CAM5, CESM1-FASTCHEM, CMCC-CM, CMCC-CMS, CNRM-CM5, GFDL-ESM2M, GISS-E2-R and NorESM1-ME. The members of group 2, the “lower correlations” group, are CSIRO-Mk3-6-0, GFDL-ESM2G, GISS-E2-H, GISS-E2-H-CC, HadCM3, Inmcm4, IPSL-CM5A-LR, IPSL-CM5A-MR, MPI-ESM-LR, MPI-ESM-P, MRI-CGCM3. Figure 4 exhibits the first and second EOF spatial results of annual-averaged precipitation anomalies (mean of 11 models) of the CMIP5 group 1 and group 2. In both groups, the percentage variation of the 1st mode is well distinguished from the 2nd mode. Though part of the ENSO precipitation signals are filtered by averaging the model members especially in the extra-tropics, both groups show ENSO-like anomaly patterns over tropical Pacific Ocean in their 1st EOF mode (Fig. 4a shading area), with the group 1 much more similar to the observations ($r \sim 0.81$) than the group 2 ($r \sim 0.53$). ENSO-related precipitation features over the extra-tropics regions are also captured by both groups, such as the positive anomalies over the northeast Pacific and the US due to the southward shift of the storm track (contours in Fig. 4a) during El Niño, the positive anomalies over the western Indian Ocean, as well as negative anomalies over the eastern tropical Indian Ocean and northern South America. However, the detailed spatial patterns of the two groups differ quite substantially from each other and from many aspects of the observations. Compared to the two observation datasets, the positive anomaly maximum center over the Pacific Ocean in group 1 is located around 180°E, as in the observational datasets, while the one in group 2 is at 150°E, leading the positive anomalies to extend too far west to the western boundary of the Pacific basin and weaken the negative anomalies over the Maritime Continent. The positive anomalies over the central Pacific Ocean in both groups appear very zonal in general and are confined meridionally from 10°S to 10°N, showing more “Hadley-like” patterns than the “Walker-like” ones in the observations (Nigam et al. 2000).

Table 2 Spatial correlation coefficients between the precipitation climatology of the 30 CMIP5 Models and observations (1901–2005, latitude weighted)

Corr.	Annual		MAM		JJA		SON		DJF	
	REC	20CR	REC	20CR	REC	20CR	REC	20CR	REC	20CR
Coefficient										
<i>CESM1-CAM5</i>	<i>0.87</i>	<i>0.87</i>	<i>0.81</i>	<i>0.79</i>	<i>0.86</i>	<i>0.85</i>	<i>0.87</i>	<i>0.87</i>	<i>0.85</i>	<i>0.85</i>
<i>CCSM4</i>	<i>0.88</i>	<i>0.88</i>	<i>0.79</i>	<i>0.79</i>	<i>0.85</i>	<i>0.85</i>	<i>0.87</i>	<i>0.87</i>	<i>0.87</i>	<i>0.86</i>
<i>CanESM2</i>	<i>0.84</i>	<i>0.87</i>	<i>0.78</i>	<i>0.81</i>	<i>0.84</i>	<i>0.84</i>	<i>0.83</i>	<i>0.85</i>	<i>0.84</i>	<i>0.86</i>
<i>CESM1-BGC</i>	<i>0.87</i>	<i>0.87</i>	<i>0.77</i>	<i>0.78</i>	<i>0.84</i>	<i>0.85</i>	<i>0.86</i>	<i>0.86</i>	<i>0.87</i>	<i>0.85</i>
<i>CESM1-FASTCHEM</i>	<i>0.86</i>	<i>0.86</i>	<i>0.78</i>	<i>0.77</i>	<i>0.84</i>	<i>0.84</i>	<i>0.85</i>	<i>0.85</i>	<i>0.86</i>	<i>0.84</i>
ACCESS1-0	0.86	0.85	0.80	0.79	0.81	0.81	0.83	0.82	0.85	0.82
ACCESS1-3	0.87	0.84	0.81	0.78	0.83	0.79	0.82	0.80	0.84	0.81
CNRM-CM5	0.81	0.82	0.74	0.76	0.80	0.81	0.82	0.84	0.80	0.81
CMCC-CMS	0.82	0.83	0.73	0.77	0.79	0.78	0.80	0.82	0.81	0.82
CMCC-CM	0.81	0.83	0.72	0.75	0.78	0.77	0.80	0.82	0.81	0.81
GFDL-ESM2M	0.80	0.80	0.71	0.72	0.78	0.77	0.79	0.80	0.80	0.78
HadGEM2-AO	0.80	0.79	0.71	0.70	0.79	0.75	0.78	0.76	0.79	0.76
GFDL-CM3	0.79	0.80	0.66	0.69	0.78	0.77	0.79	0.79	0.78	0.79
NorESM1-ME	0.79	0.79	0.71	0.71	0.73	0.74	0.79	0.78	0.76	0.74
GISS-E2-R	0.77	0.77	0.74	0.73	0.70	0.72	0.78	0.78	0.76	0.75
GFDL-ESM2G	0.77	0.75	0.70	0.68	0.77	0.75	0.78	0.78	0.78	0.75
HadCM3	0.77	0.73	0.72	0.68	0.74	0.70	0.79	0.75	0.78	0.74
NorESM1-M	0.79	0.79	0.70	0.70	0.73	0.75	0.79	0.78	0.76	0.74
MIROC5	0.79	0.76	0.76	0.76	0.75	0.73	0.79	0.77	0.74	0.73
GISS-E2-R-CC	0.77	0.77	0.73	0.73	0.70	0.71	0.78	0.78	0.76	0.75
CSIRO-Mk3-6-0	0.74	0.75	0.67	0.69	0.71	0.72	0.76	0.77	0.73	0.73
inmcm4	0.75	0.76	0.73	0.74	0.68	0.69	0.70	0.71	0.77	0.78
IPSL-CM5A-LR	0.74	0.74	0.66	0.68	0.73	0.71	0.76	0.76	0.74	0.72
IPSL-CM5A-MR	0.74	0.74	0.66	0.69	0.72	0.69	0.75	0.75	0.73	0.73
MRI-CGCM3	0.73	0.74	0.65	0.64	0.73	0.70	0.74	0.74	0.69	0.68
GISS-E2-H-CC	0.73	0.72	0.69	0.69	0.64	0.66	0.74	0.73	0.71	0.69
MPI-ESM-LR	0.71	0.71	0.62	0.67	0.69	0.69	0.76	0.76	0.69	0.69
GISS-E2-H	0.73	0.72	0.68	0.69	0.64	0.65	0.73	0.72	0.71	0.70
IPSL-CM5B-LR	0.71	0.73	0.59	0.61	0.68	0.67	0.72	0.73	0.71	0.69
MPI-ESM-P	0.71	0.71	0.62	0.67	0.69	0.68	0.76	0.75	0.68	0.68

Group 1 models are marked in italic; group 2 models are marked in bold

In the group 2, the positive anomalies pattern is even narrower and longer than in group 1, showing a more “Hadley-like” pattern. The precipitation climatology (contours in Fig. 4a) is strongly related to the details of the ENSO-related precipitation anomalies. As group 2 has more severe “dry equator” and “double-ITCZs” biases, it also exhibits much more obvious near-zero anomaly equator and double positive anomaly bands over the tropical eastern Pacific Ocean in the first EOF mode. Although less severe, group 1 also shows “double-ITCZs” in its precipitation climatology and a related positive anomaly band in its ENSO precipitation pattern. For the SPCZ biases, group 2 with a less tilted SPCZ in the annual-averaged precipitation climatology exhibits less positive anomalies over the central tropical and the southeastern Pacific Ocean. In

general, the precipitation climatology (contours in Fig. 4a) confines the shape of the ENSO-related precipitation pattern (shaded areas) more in the models than in the observations (Fig. 3a), which may indicate that the precipitation background in the models has greater impact on its ENSO-related precipitation spatial patterns.

In the 2nd EOF mode (Fig. 4b), group 1 exhibits a region of positive anomalies in the far western Pacific Ocean and the Maritime Continent, similar to the observations ($r \sim 0.65$), while the result of group 2 is more zonal and “Hadley-like” (Nigam et al. 2000). Overall, the CMIP5 models, especially the group 1, demonstrate the ability to simulate ENSO-like precipitation anomalies mean state features that are similar to the observations, though detailed patterns are different.

Table 3 Spatial correlation coefficients between the first EOF mode spatial fields of precipitation anomalies of 30 CMIP5 models and observations (1901–2005, latitude weighted)

Corr.	Annual		JJA		DJF	
	REC	20CR	REC	20CR	REC	20CR
Coefficient						
<i>CESM1-CAM5</i>	<i>0.72</i>	<i>0.69</i>	<i>0.69</i>	<i>0.75</i>	<i>0.66</i>	<i>0.65</i>
<i>GFDL-ESM2M</i>	<i>0.77</i>	<i>0.76</i>	<i>0.63</i>	<i>0.61</i>	<i>0.75</i>	<i>0.69</i>
<i>CMCC-CMS</i>	<i>0.80</i>	<i>0.78</i>	<i>0.70</i>	<i>0.61</i>	<i>0.76</i>	<i>0.79</i>
<i>CNRM-CM5</i>	<i>0.59</i>	<i>0.50</i>	<i>0.70</i>	<i>0.66</i>	<i>0.82</i>	<i>0.82</i>
<i>CESM1-FASTCHEM</i>	<i>0.75</i>	<i>0.74</i>	<i>0.64</i>	<i>0.74</i>	<i>0.68</i>	<i>0.66</i>
<i>CESM1-BGC</i>	<i>0.75</i>	<i>0.72</i>	<i>0.66</i>	<i>0.72</i>	<i>0.68</i>	<i>0.68</i>
<i>NorESM1-ME</i>	<i>0.76</i>	<i>0.75</i>	<i>0.56</i>	<i>0.68</i>	<i>0.73</i>	<i>0.72</i>
NorESM1-M	0.71	0.72	0.54	0.67	0.77	0.74
MIROC5	0.75	0.74	0.60	0.60	0.67	0.64
IPSL-CM5B-LR	0.77	0.71	0.56	0.45	0.77	0.73
CCSM4	0.73	0.72	0.62	0.74	0.69	0.68
GISS-E2-R-CC	0.69	0.74	0.52	0.58	0.71	0.69
<i>CanESM2</i>	<i>0.53</i>	<i>0.55</i>	<i>0.59</i>	<i>0.63</i>	<i>0.65</i>	<i>0.61</i>
<i>GISS-E2-R</i>	<i>0.67</i>	<i>0.73</i>	<i>0.48</i>	<i>0.56</i>	<i>0.73</i>	<i>0.71</i>
<i>CMCC-CM</i>	<i>0.63</i>	<i>0.72</i>	<i>0.52</i>	<i>0.46</i>	<i>0.74</i>	<i>0.78</i>
GISS-E2-H-CC	0.49	0.51	0.51	0.58	0.54	0.51
GFDL-CM3	0.42	0.44	0.38	0.47	0.61	0.57
ACCESS1-0	0.42	0.49	0.43	0.42	0.63	0.58
ACCESS1-3	0.57	0.53	0.43	0.36	0.55	0.52
GISS-E2-H	0.48	0.48	0.44	0.46	0.49	0.47
MRI-CGCM3	0.58	0.46	0.52	0.42	0.51	0.43
MPI-ESM-LR	0.49	0.41	0.44	0.47	0.32	0.30
HadCM3	0.43	0.46	0.31	0.22	0.59	0.56
IPSL-CM5A-MR	0.38	0.40	0.40	0.39	0.45	0.47
inmcm4	0.43	0.42	0.37	0.34	0.40	0.38
MPI-ESM-P	0.47	0.40	0.40	0.49	0.34	0.31
HadGEM2-AO	0.47	0.49	0.19	0.11	0.59	0.55
GFDL-ESM2G	0.38	0.34	0.42	0.45	0.30	0.28
IPSL-CM5A-LR	0.36	0.35	0.36	0.35	0.36	0.38
CSIRO-Mk3-6-0	0.35	0.30	0.34	0.37	0.28	0.24

Group 1 models are marked in italic; group 2 models are marked in bold

4.2 Seasonally-averaged precipitation anomalies EOF results

4.2.1 REC and 20CR

We use EOF analysis on both 15-year filtered JJA- and DJF-averaged precipitation anomalies, in order to further compare the spatial patterns of seasonally-averaged ENSO-related precipitation in the CMIP5 models and the observations. The observational JJA EOF 1st mode results (Fig. 5a) show that the 20CR exhibits larger positive anomalies over the eastern Pacific than the REC and the maximum positive anomaly in the 20CR shifts to the east of 180°E by about 15°. The REC JJA maximum center, however, is located in the same position as the annual-averaged EOF result

(Fig. 3). The positive anomalies at the summer Indian monsoon region in the 20CR are also larger than the ones in the REC and connect with the positive anomalies over western tropical Pacific. This might be due to the fact that the JJA Indian monsoon is much stronger in the 20CR than the REC (contours in Fig. 5a). Another major difference is that, unlike the REC, the positive anomalies over the central tropical Pacific Ocean are separate from the ones over the southeast Pacific Ocean in 20CR. In DJF 1st EOF results (Fig. 5b), the ENSO-related positive precipitation anomaly centers are much larger than both the annual and the JJA ones, consistent with the finding that the peak phase of ENSO generally occurs in boreal winter (e.g. Rasmusson and Carpenter 1982; Trenberth and Caron 2000). The ENSO-related pattern in the 20CR closely resembles that in the REC

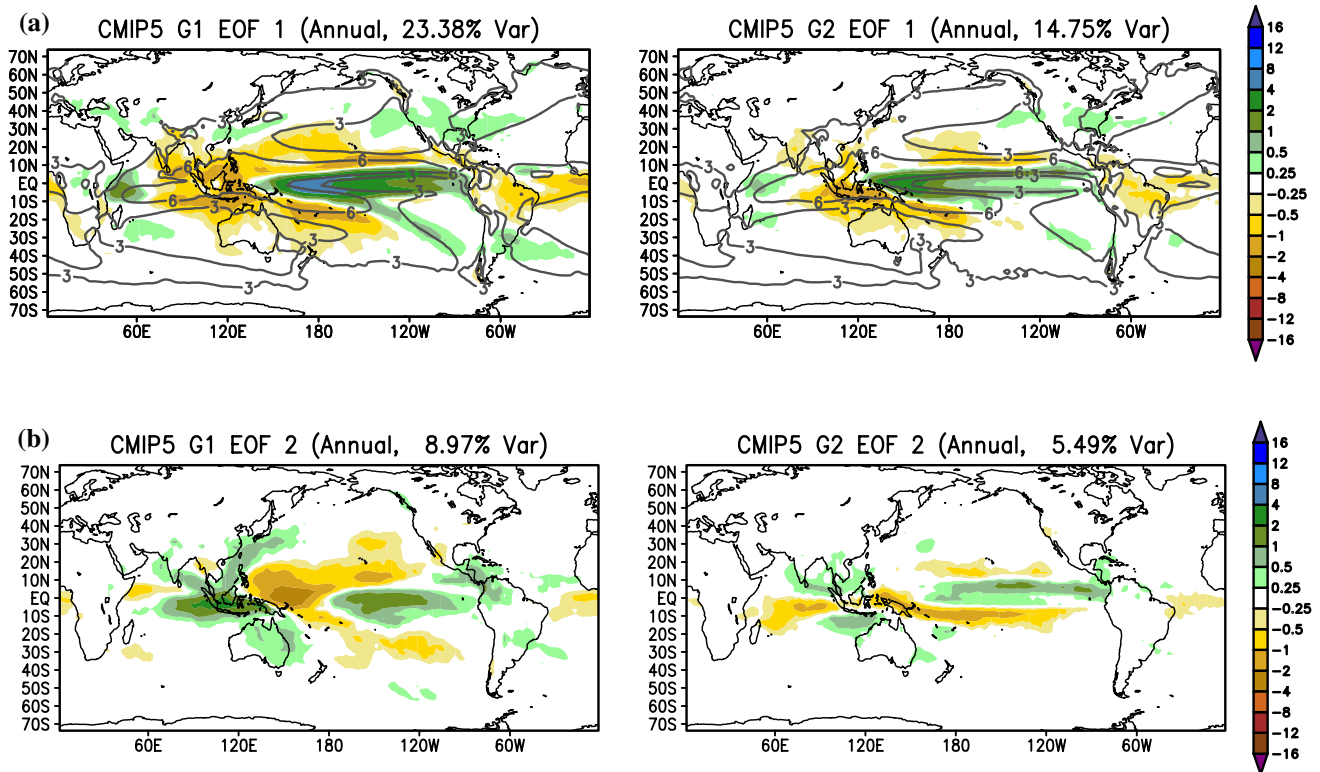


Fig. 4 EOF first and second mode spatial results of the mean of the CMIP5 group 1 and 2 models precipitations anomalies (mm/day, 1901–2005) (mean of ensemble members of each model) (*shading*

is the precipitation anomalies EOF results; contours are the annual-averaged precipitation climatology of 3 and 6 mm/day). **a** First EOF mode, **b** second EOF mode

($r_{\text{DJF}} = 0.89 > r_{\text{JJA}} = 0.87$ and $r_{\text{Annual}} = 0.88$), though 20CR has a slightly stronger maximum positive anomaly center over the tropical Pacific. One possible explanation for these differences is that both the DJF ITCZ and the DJF SPCZ (contours in Fig. 5b) in the 20CR are stronger than the REC while Southeast Asia is drier in the 20CR. Therefore, during El Niño when the SPCZ in the 20CR moves northeastward and merges with the ITCZ (Meehl 1987; Vincent 1994), larger positive anomalies accumulate over the central Pacific. Other detail differences such as the previously mentioned drier anomalies in the 20CR over the eastern off-equator Pacific, the northeastern Atlantic Ocean and the Indian Ocean at 10°S also exist in both the JJA and the DJF results, suggesting that these differences result from some fundamental disagreements between the two datasets. The time series of first modes of the observations correlate well in DJF (Fig. 5b), with the REC exhibiting larger positive and negative deviations in the second half of century than the 20CR. Our preliminary study suggests this difference may reside in the power of the 1–15 years period, which is about 4 times smaller in the DJF-averaged 20CR than the REC. Therefore, the increasing variability of the 20CR EOF time series may not be large enough to be shown in the 1st EOF mode, but in the 2nd EOF mode instead.

4.2.2 CMIP5 models

The spatial patterns of CMIP5 JJA EOF mode 1 (Fig. 6a) are more similar to those of 20CR than the REC, with the positive anomaly centers over the central Pacific Ocean being separated from the southeastern ones by negative anomalies. The positive anomalies associated with the Southeast Asian Monsoon also connect with those in the western Pacific rainfall region in both groups. The differences between these two groups still exist. The JJA maximum positive anomaly center of the group 1 shifts to the east of 180°E, same as the 20CR, while the one of group 2 still locates at 150°E. Both groups show that the biases of the JJA double positive anomaly bands over the eastern Pacific are less severe than the ones in the annual-averaged EOF results (Fig. 4a). This is related to the less strong “southern-ITCZs” in the JJA precipitation climatology (contours in Fig. 6a) in the models. Group 2 still exhibits stronger “double-ITCZs” in its JJA-averaged precipitation climatology than group 1, with associated stronger double anomaly bands over the eastern Pacific Ocean.

For CMIP5 DJF EOF results, Table 3 indicates that the DJF pattern correlations between CMIP5 models and the two observation datasets (multi-model ensemble mean

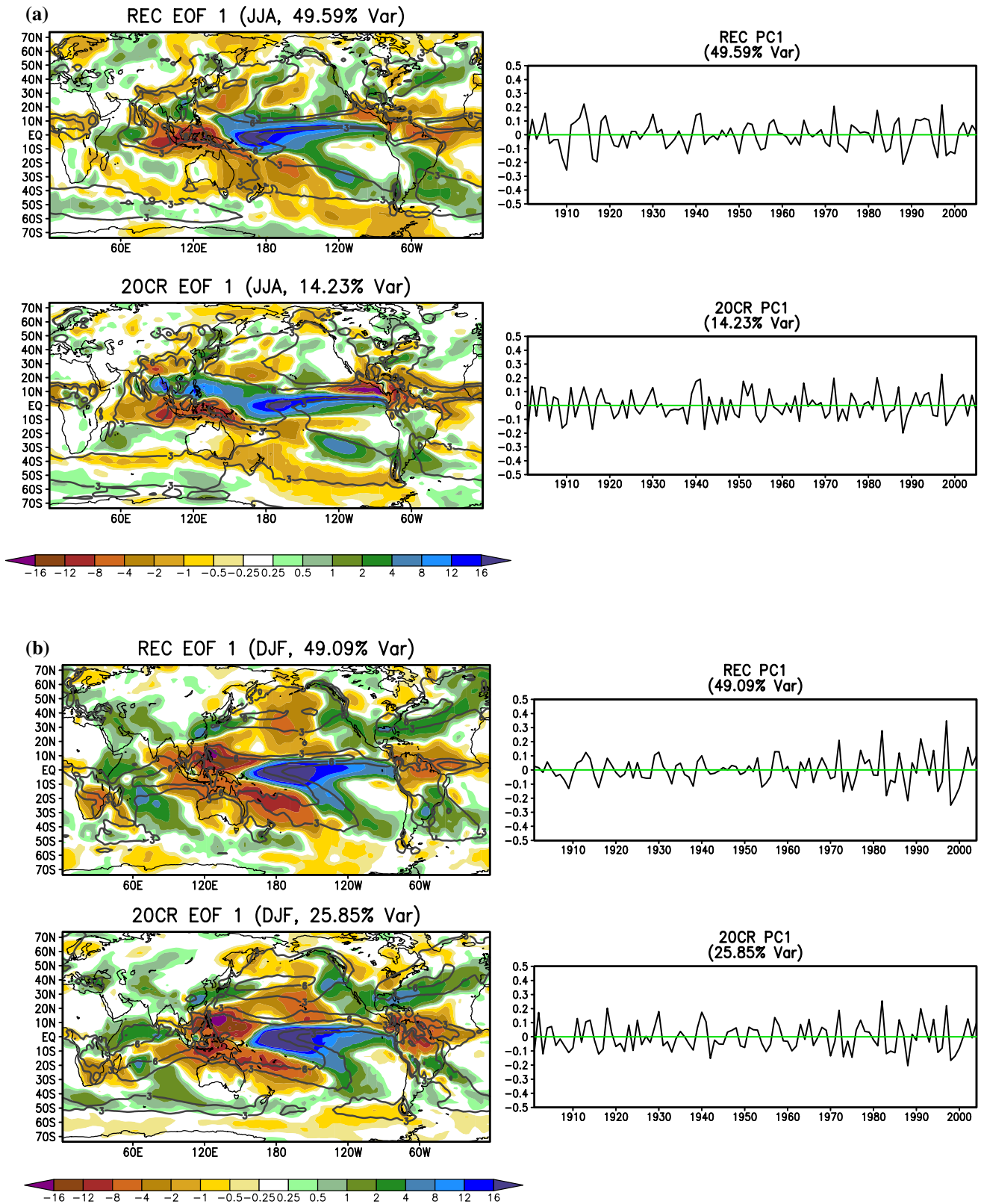


Fig. 5 First and second EOFs of the 2 observational datasets **a** JJA-averaged precipitations anomalies (mm/day, 1901–2005), **b** DJF-averaged precipitations anomalies (mm/day, 1901–2005) (*shading is*

the precipitation anomalies EOF results; contours are the JJA-/DJF-averaged precipitation climatology of 3 and 6 mm/day)

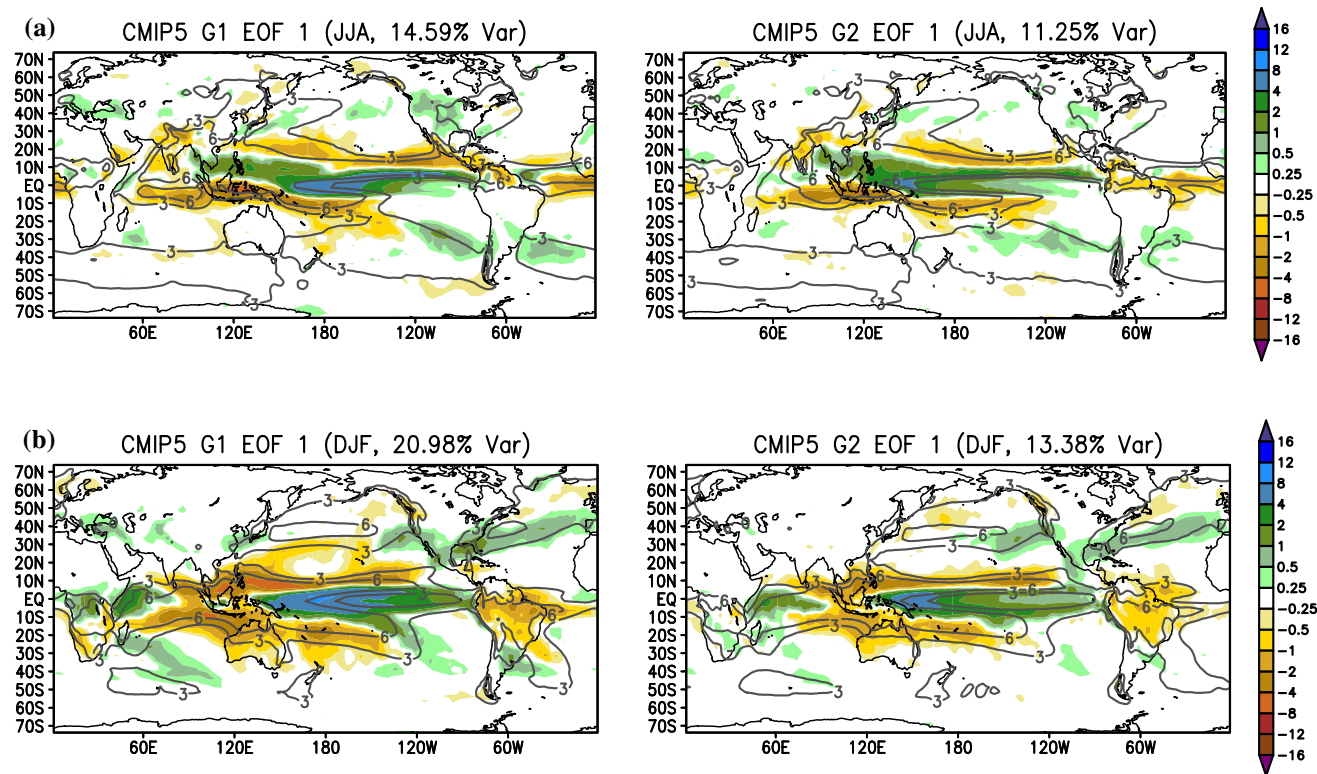


Fig. 6 First EOF of the mean of the CMIP5 groups 1 and 2 models JJA- and DJF-averaged precipitations anomalies (mm/day, 1901–2005) (shading is the precipitation anomalies EOF results; contours

are the JJA-/DJF-averaged precipitation climatology of 3 and 6 mm/day). **a** JJA EOF first mode, **b** DJF EOF first mode

of correlation coefficients $r \sim 0.58$) are generally higher than the JJA ones ($r \sim 0.51$), and are in the same range as the annual ones ($r \sim 0.58$). In both CMIP5 groups, the DJF first EOF modes (Fig. 6b) show that the maximum anomaly centers are stronger in DJF than in JJA and the annual mean, as the SPCZs become stronger from JJA to DJF, moving northeastward and merging with the ITCZ. The models also capture the features that are similar to the observations, such as the increasing DJF-averaged extratropical positive anomalies related to the northern storm tracks. The differences between the two CMIP5 models, such as the locations of the maximum anomaly centers as well as the narrower positive anomalies pattern in group 2, are also very obvious in Fig. 6b. For both groups, the maximum negative anomalies extend zonally just north of the positive anomalies over the tropical Pacific, different from the “Walker-like” patterns of the observations. Since the “southern-ITCZs” biases are more severe in models’ DJF precipitation climatology (contours in Fig. 6b), group 2 has larger positive anomalies over the southern off-equator than the ones over the northern off-equator in the eastern Pacific Ocean. On the other hand, the strong “southern-ITCZs” and the resulting less severe “dry equator” in the DJF precipitation climatology lead to the reduced bias of the near

zero anomaly bands over the eastern Pacific in the group 2 DJF EOF results.

5 El Niño and La Niña composites

In order to examine separately the details of El Niño and La Niña precipitation variability, we use El Niño/La Niña composites calculated from the REC, the 20CR and the 2 CMIP5 groups. The spatial pattern of ENSO composite precipitation anomalies (in this case, we use El Niño minus La Niña to represent ENSO) in each datasets correlates very well with its own EOF first mode result for all the annual, JJA and DJF results, with all the correlation coefficients greater than 0.9. This is another indication of the ability of the 30 CMIP5 models to simulate ENSO, since the largest covariance (the leading mode) in the EOF method might not contain all the ENSO signals.

We present in Fig. 7 the annually-, JJA- and DJF-averaged El Niño precipitation composite maps of the REC along with the spatial differences between the two observations in El Niño precipitation composites results. In annual averaged El Niño results of the REC, a typical magnitude for its maximum positive anomaly center over the tropical

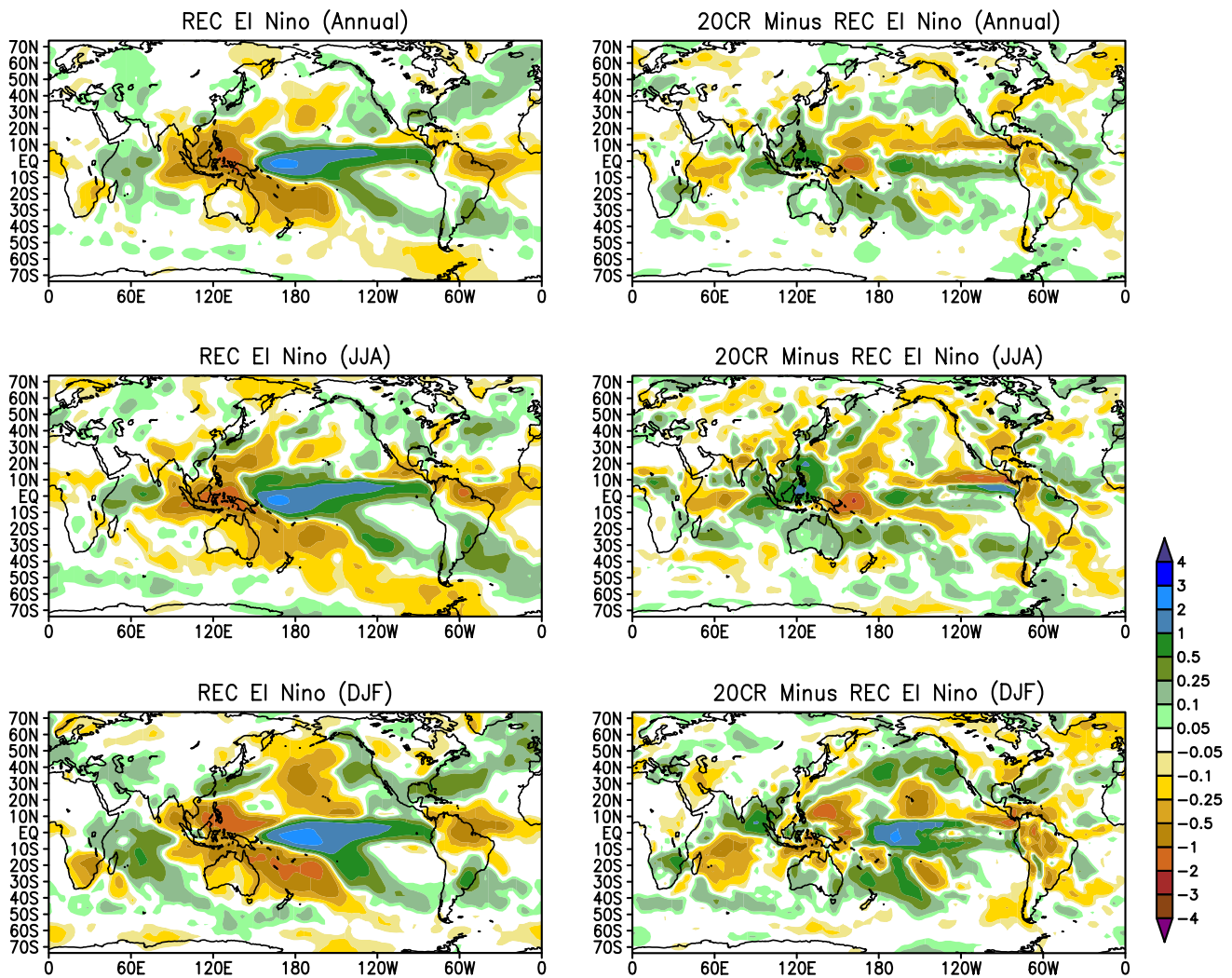


Fig. 7 Annual-(upper panel), JJA-(middle panel) and DJF-(lower panel) averaged El Niño-related precipitation composites maps of the REC (left column) and the difference maps between the REC and the 20CR (right column) (mm/day, 1901–2005)

Pacific Ocean is about 2–3 mm/day, and the maximum negative anomaly center over the Maritime Continent is about –2 to –1 mm/day. Due to a slightly more eastward maximum anomaly center, the 20CR is wetter over the Maritime Continent by 0.5–1 mm/day and the central to eastern tropical Pacific in the Southern Hemisphere, while being drier over the eastern Maritime Continent and the central to eastern Pacific Ocean in the northern tropics. The La Niña composites and difference results (not shown) are in the opposite sense. In JJA, positive anomaly center of the REC over tropical Pacific slightly decreases while the negative anomaly center over the Maritime Continent expands. The 20CR exhibits larger positive (negative) anomalies near the equator in the central to eastern Pacific and drier (wetter) anomalies over the SPCZ region in its El Niño (La Niña) results. In the DJF El Niño composite result, the maximum positive anomaly center reaches its peak, though the

magnitude range is still 2–3 mm. The DJF difference map shows that the 20CR has more (less) precipitation over the central Pacific Ocean and less (more) over the western Pacific in El Niño (La Niña) situations, which indicate that the 20CR has stronger DJF El Niño (La Niña) -related precipitation (drought) than the REC. In summary, compared to the REC, the 20CR precipitation anomalies in the central Pacific Ocean are larger in DJF and El Niño mode, with other seasons and La Niña mode being drier, except over the “southern-ITCZ” regions in the eastern Pacific where 20CR tends to have more precipitation than REC across the seasons.

For the CMIP5 El Niño precipitation composite results, we display model agreement maps on the same sign of El Niño-related precipitation biases from the two observations in Fig. 8 (La Niña results are almost opposite). Most of the 30 models (Fig. 8a) exhibit positive biases over the

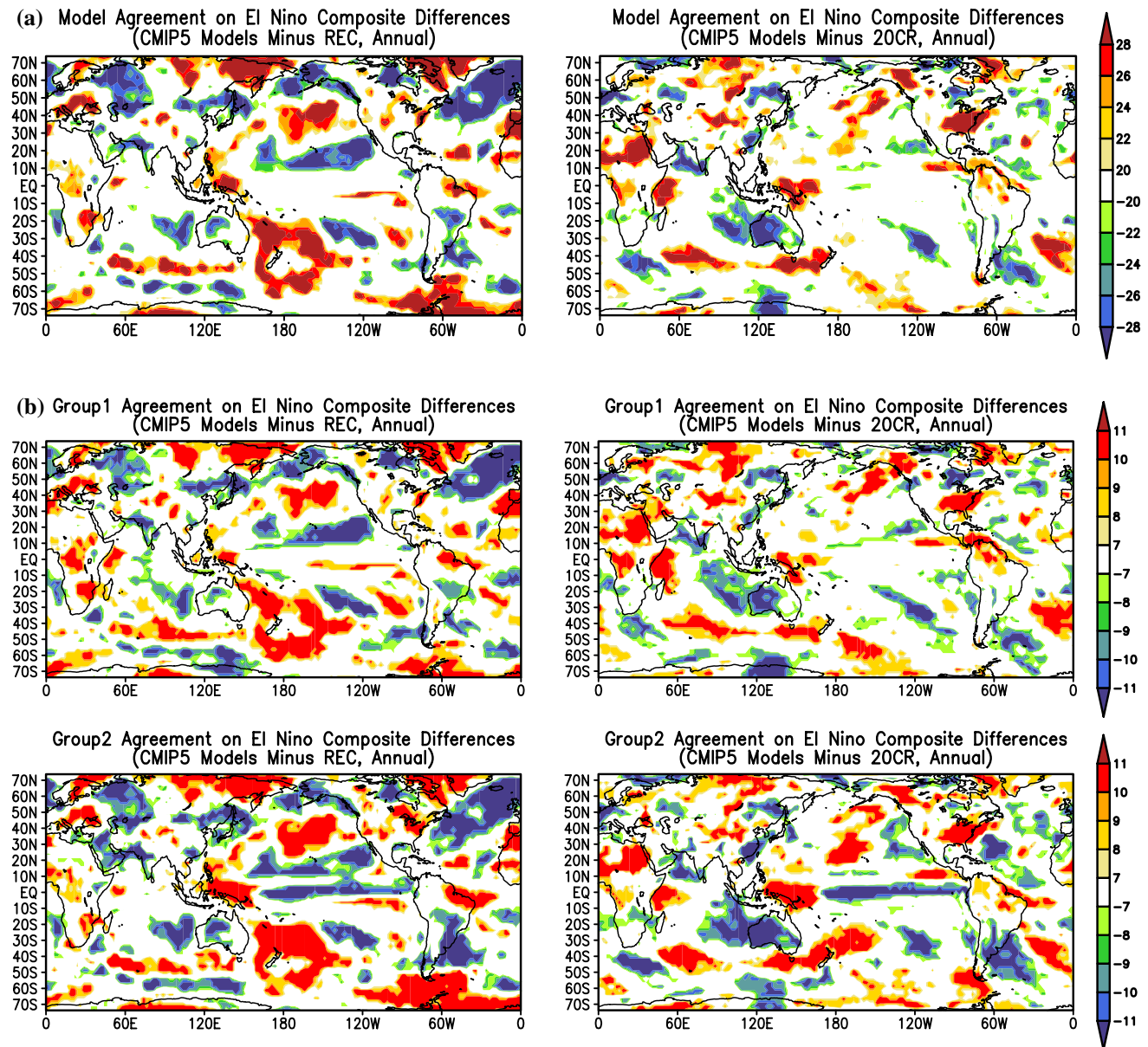


Fig. 8 **a** Agreement among the 30 CMIP5 models on annual-averaged El Niño-related precipitation composites biases with the 20CR and the REC. **b** Same as **a**, but among the 2 CMIP5 groups (each group has 11 members). Red (blue) color or positive (negative) value

at each grid point represents the number of models that have positive (negative) El Niño-related precipitation anomaly biases from the observations

western tropical Pacific and Indian Ocean, the north central Pacific, the Southern Hemisphere storm track and eastern North America. Highly consistent negative biases are found over the southeastern Indian Ocean and western Australia, as well as the southern central Pacific where the observed anomalies associated with the SPCZ southern end are located. Among these biases, the positive ones over the western tropical Pacific and Indian Ocean as well as the negative ones over the southeastern Indian Ocean and SPCZ region are seasonally consistent. In the grouped models

agreement maps (Fig. 8b), consistent negative biases over the equatorial Pacific and southern South America are the specific features for the group 2. In addition, group 2 models exhibit more positive biases of ENSO-related precipitation anomalies over the western tropical Pacific and extratropical central Pacific in both hemispheres. All the other biases mentioned above also appear on both group 1 and 2 agreement maps, suggesting that these biases are the most common ones among the CMIP5 models for ENSO-related precipitation. The bias of the double positive anomaly

bands associated with the “double-ITCZs” in the models are more obvious when comparing with the REC than the 20CR, indicating that this bias might be more sensitive to the number of observations than the one of near zero equatorial anomaly band that is related to the “dry equator”.

To further quantitatively compare the El Niño- and La Niña- related precipitation signals in observations and models, we use the “moving block average” method introduced by Curtis and Adler (2000) using El Niño- and La Niña- related precipitation composites results. The results (Fig. 9 upper panel) show that both the El Niño- and La Niña- related precipitation signals in the majority of CMIP5 models are weaker than those in the two observation datasets. This might be due to the fact that the models’ maximum (minimum) anomalies centers in El Niño (La Niña) phase are located more westward than those in the observations and are out of the Pacific box. Another factor is that dry (wet) anomalies of the El Niño (La Niña) phase in models are generally too weak compared to the observations. In spite of the weaker ENSO signals in models, most models exhibit stronger ENSO-related precipitation signals in DJF just as the observations. The models that have more severe “dry equator” problems in Fig. 2 exhibit less seasonal variability of ENSO-related precipitation signals. Figure 9 middle panel shows the variation in magnitudes and seasonal variability of the ENSO precipitation index between the two CMIP5 groups. Group 1 has mean value (2.8 mm/day for El Niño) and seasonal variability (2.3 mm/day for El Niño, maximum minus minimum) on the same level as the two observation datasets in both El Niño and La Niña phases, while the group 2 has much lower mean value (1.1 mm/day for El Niño) and seasonal variability (0.6 mm/day for El Niño). The ENSO nonlinearity, which is the differences between El Niño and La Niña phases, is also smaller in the CMIP5 group 2 than the group 1.

In addition, normalization of the ENSO precipitation index by the corresponding ENSO SST variability is calculated in order to study how the ENSO SST variability influences the ENSO-related precipitation extremes. The El Niño (La Niña) SST variability is defined by the SD of positive (negative) values of SST 1st EOF time series. After dividing the El Niño/La Niña precipitation indexes by the corresponding SST variability, the normalized index values generally become slightly larger (Fig. 9 bottom panel). The seasonal variability of normalized El Niño precipitation indexes for both CMIP5 group 1 and 2 are identical to those in the Fig. 9 middle panel. The normalized La Niña indexes are also very similar to those in the Fig. 9 middle panel, with the group 1 mean values becoming obviously smaller than the observations after the normalization, especially in DJF. Therefore, it is possible that the ENSO SST variability exerts larger influence on the DJF La Niña-related precipitation extremes than the El Niño ones. The

ENSO-related precipitation in CMIP5 group 1 models is also more susceptible to the ENSO SST variability than the group 2 ones.

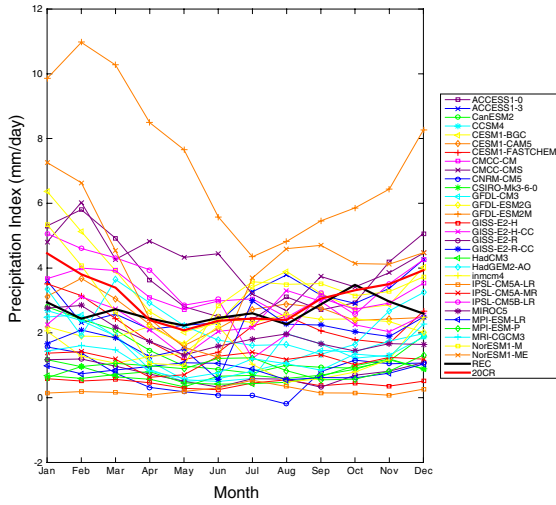
6 Discussion and summary

The above results indicate that the precipitation climatology biases influence the ENSO-related precipitation anomaly biases. In addition, the variability of ENSO-related SST anomalies exerts some impact on the ENSO-related precipitation ones. This section further discusses the detailed connections between the biases of precipitation climatology/ENSO-related SST and those of ENSO-related precipitation.

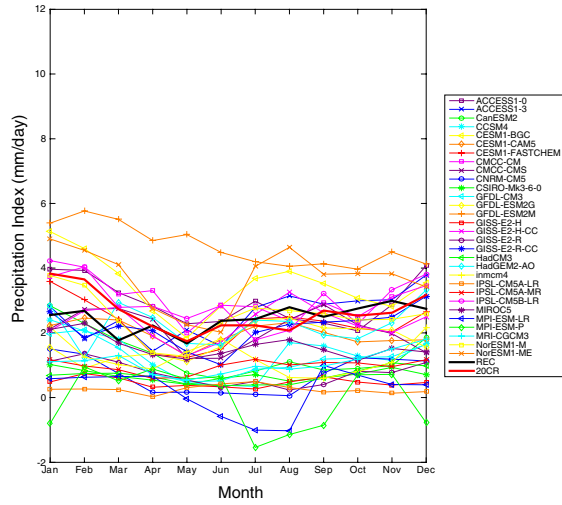
The connections between the biases of precipitation climatology and ENSO-related precipitation anomalies are indicated by agreement maps among the CMIP5 models on same sign shared by precipitation climatology biases and biases in El Niño-related precipitation (Fig. 10). In the 30 CMIP5 models agreement map (Fig. 10a), the connections between the positive biases of mean state precipitation and the positive ones of the El Niño precipitation over the Maritime Continent and the western Indian Ocean are the only areas with high agreements among the models. The grouped agreement results (Fig. 10b) support this result. In addition, the group 2 models show strong agreement on the relation between the “dry equator” bias of precipitation climatology and the bias of the near zero anomaly band over the Pacific equator in El Niño-related precipitation. The effect of the “double-ITCZs” on the double anomaly bands over the eastern Pacific previously discussed is consistent among models on the biases agreement map for the REC, but in the 20CR this effect/relation is not as clear. This further indicates that the effect of the “dry equator” bias on ENSO-related precipitation is less sensitive to the observational reference than that of the “double-ITCZs”.

In order to further investigate the influence of SST anomalies on the ENSO-related precipitation patterns, a singular value decomposition (SVD) analysis (Bretherton et al. 1992) is used in this study. This method searches for the coupled patterns of precipitation and SST that are co-varying in time. The SVD first mode homogeneous correlation (temporal correlations between normalized SST and normalized ENSO-related SST) maps are presented in Fig. 11 for SST and heterogeneous correlation ones (temporal correlations between normalized precipitation and normalized ENSO-related SST) for the precipitation. In Fig. 11a, the response of ERSST to the ENSO time series (ERSST first SVD mode) strongly resembles that of HadISST. The correlations of the normalized REC precipitation field and the ERSST SVD first time series are much higher at most grid points than the 20CR-HadISST ones due to the

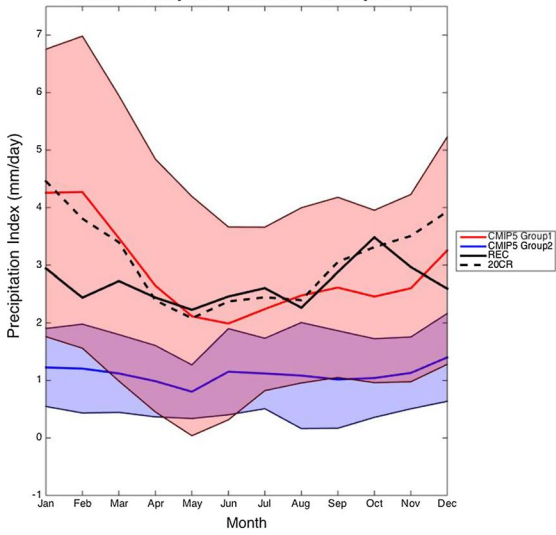
El Niño Precipitation Index Intermodel Comparison



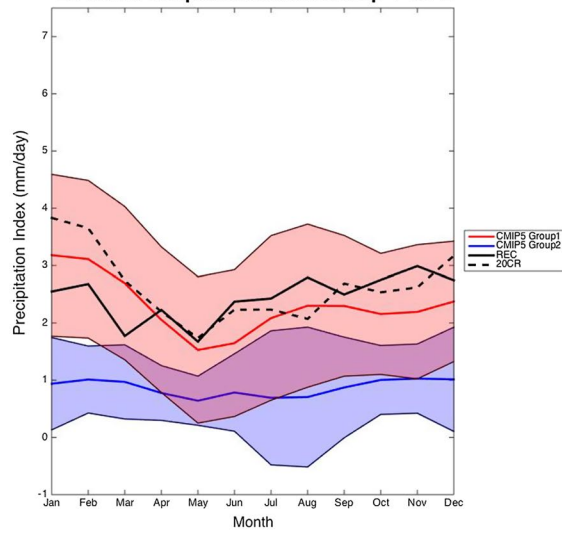
La Niña Precipitation Index Intermodel Comparison



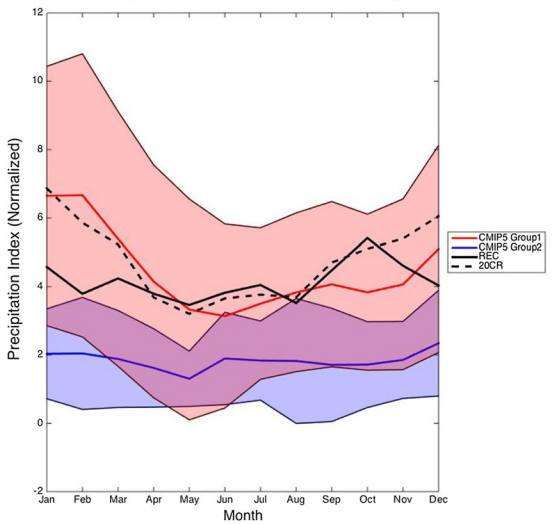
El Niño Precipitation Index Group 1 VS 2



La Niña Precipitation Index Group 1 VS 2



El Niño Precipitation Index Group 1 VS 2 (Normalized)



La Niña Precipitation Index Group 1 VS 2 (Normalized)

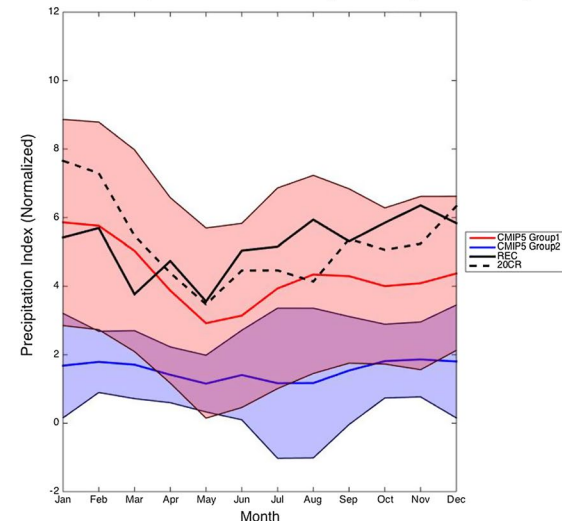


Fig. 9 Upper panel El Niño and La Niña precipitation signal comparisons among the 20CR, the REC and the 30 CMIP5 models (mm/day, 1901–2005); middle panel El Niño and La Niña precipitation signals of the 20CR, the REC and the two CMIP5 groups (shading area stands for the positive/negative SD; mid-line stands for the mean of each group); bottom panel normalized results of the middle panel using SD of monthly-averaged SST EOF 1st time series in each dataset

fact that REC is reconstructed based on the covariance of ERSST, though both correlation patterns are very similar

to the ENSO-related precipitation ones from the EOF first mode results (Fig. 3a).

Both of the CMIP5 groups exhibit the ability to simulate ENSO-like SST and precipitation patterns (Fig. 11b). However, for group 2, these patterns are shown in the second SVD mode rather than in the first one as for group 1. The ENSO SST correlation pattern of the group 1 are much more similar to the observational ones, with the same meridional width of positive correlations in the Pacific Ocean. The positive ENSO-related SST correlations of the

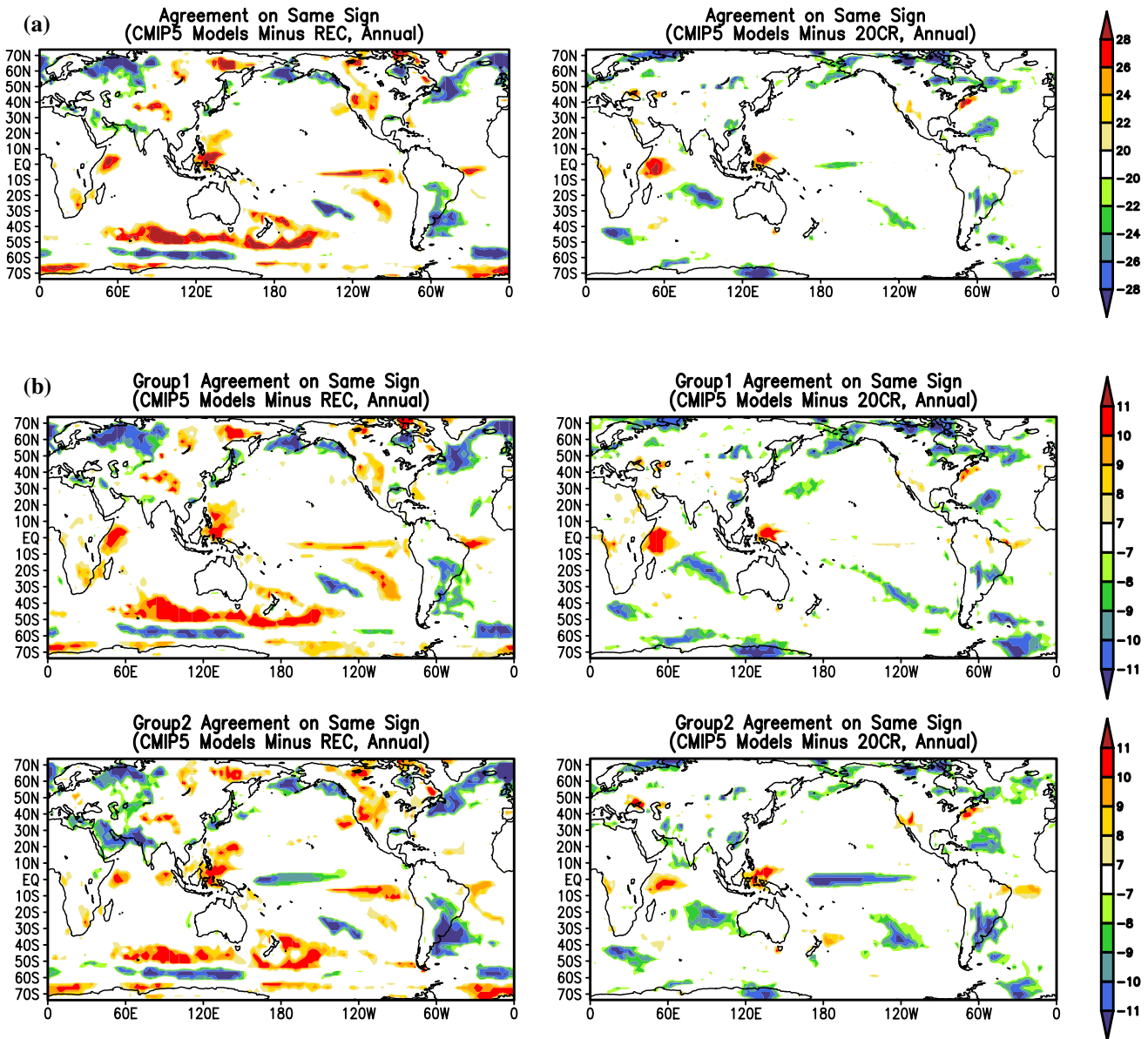


Fig. 10 a Agreement among the 30 CMIP5 models on same sign (positive or negative) shared by the annual-averaged precipitation climatology biases and the annual-averaged ENSO-related precipitation composites biases from the 20CR and the REC. b Same as a, but among the 2 CMIP5 groups (each group has 11 members). Red

(blue) color or positive (negative) value at each grid point represents the number of models that have positive (negative) biases for both of precipitation climatology and ENSO-related precipitation anomalies when compared with REC/20CR

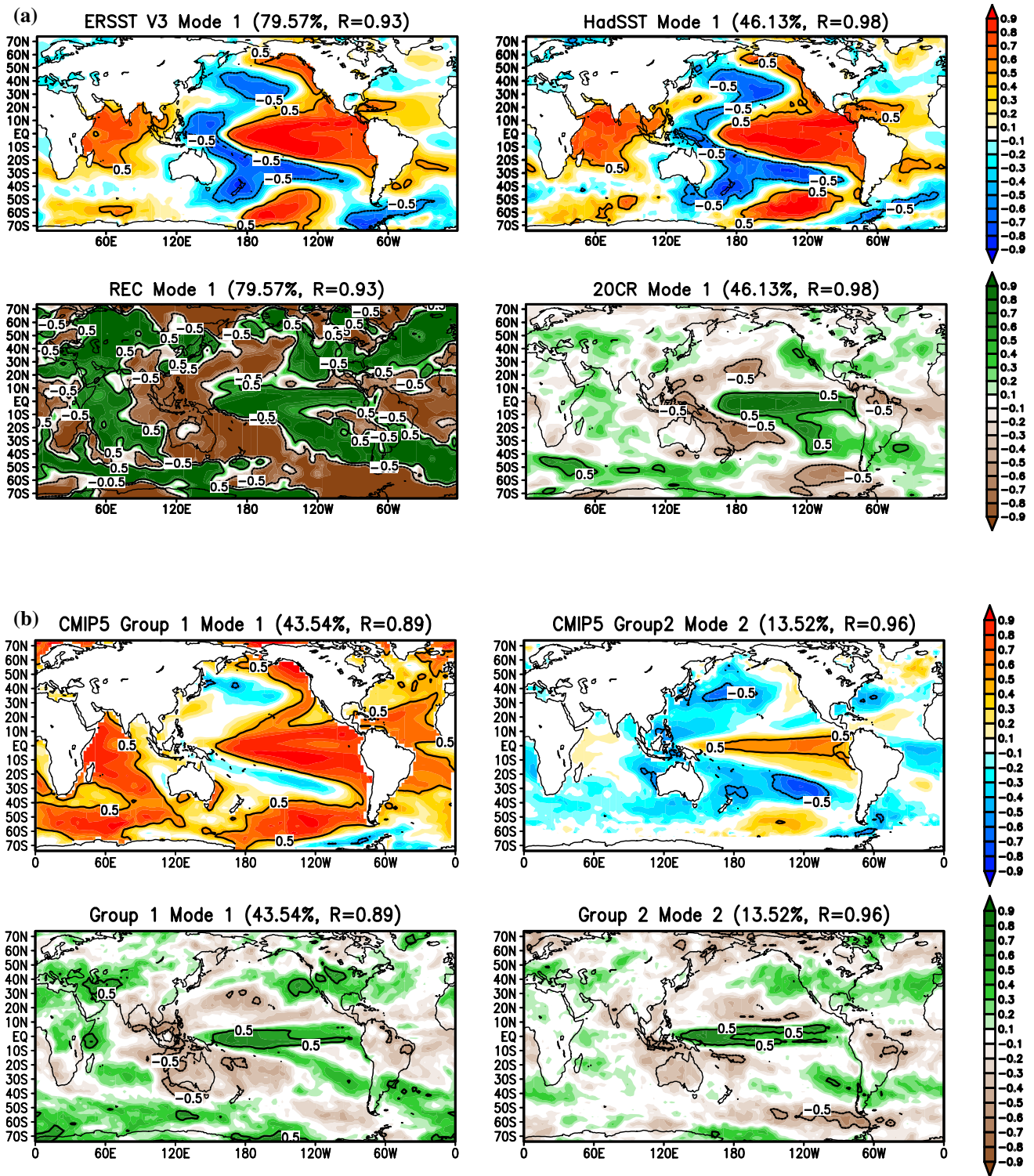


Fig. 11 Annual-averaged SVD mode 1 or 2 (see text) of **a** the observations and **b** the 2 CMIP5 groups. *Upper panel* homogenous temporal correlation maps for the normalized SST; *lower panel* heterogeneous temporal correlation maps for the normalized precipitation.

Percentage stands for the explained total variance of this SVD mode; R stands for the temporal correlation coefficient between SVD time series of SST and precipitation

Indian Ocean, the Atlantic Ocean and the southern Pacific Ocean are generally larger than both observations, while the negative ones in the western and extratropical Pacific Ocean are generally smaller. Comparing to the group 1, the positive SST correlation pattern in the group 2 is slightly more westward extended and meridionally narrower, resulting in a more westward-extended and narrower ENSO-like pattern in the precipitation heterogeneous correlation field. Both CMIP5 groups have higher correlations in the southern “double anomaly band” region, suggesting that double anomaly band biases of the ENSO-related precipitation in the models and the related “double-ITCZs” problems may have connections with the ENSO-related SST temporal variations. The normalized precipitation over the equator in the models is less correlated with the normalized ENSO SST, indicating that the variability of the precipitation over this region may be more related to their precipitation climatology rather than the ENSO variability. This result further confirms that there are strong connections between the “dry equator” in precipitation climatology and the near zero equatorial anomaly band in ENSO-related precipitation that is discussed above.

In this paper, we compare the spatial patterns of the 1901–2005 precipitation climatology, the precipitation EOF results, as well as the ENSO precipitation composites results among the 20CR, the REC and the 30 CMIP5 models. The precipitation climatology results show that though the REC is drier than the 20CR by an average of 0.50 mm/day, their seasonal- and annual-averaged precipitation patterns are alike. The 30 CMIP5 models all have relatively good spatial correlation with the two observations, but biases such as the dry equator, “double-ITCZs” in eastern tropical Pacific, an overly zonal and eastward-extended SPCZ are quite obvious. The “double-ITCZs” problem is most severe in DJF due to the strong and eastward-extended SPCZ. There are other shared precipitation biases among the models compared to the 20CR and the REC, e.g. overestimated precipitation over the tropical Atlantic and Indian Ocean, Maritime Continent, northern Pacific subtropical high region, central and southern Africa and Australia; underestimated rainfall over northern extra-tropical storm track region, central America and tropical South America and central United States.

The EOF and ENSO composites results show that the spatial fields of the REC and the 20CR correlate with each other very well. The 30 CMIP5 models also show statistically meaningful spatial correlations with the REC and the 20CR. However, the “dry equator” and “double-ITCZs” biases in the model precipitation climatologies are primarily responsible for the lower correlations between modeled and observed climatologies and ENSO-related precipitation anomalies. Two groups of models are selected based on their higher (lower) correlations with the observations

in precipitation climatology and EOF-related precipitation. Both groups have the ability to reproduce ENSO-like features of precipitation anomalies that are similar to the observations, from both annually and seasonally averaged perspectives. Overall, the group 1 performs better than the group 2 in the spatial patterns of ENSO-related precipitation, the mean magnitude and the seasonal variability of ENSO precipitation signals, as well as the SST/precipitation correlation patterns produced from the SVD analyses. However, the ENSO-related precipitation patterns of the models share common biases such as the positive anomalies over tropical Pacific Ocean in the CMIP5 models extend too far west and are meridionally narrower than the observations, exhibiting more “Hadley-like” than “Walker-like” patterns. The detailed ENSO-related precipitation spatial patterns in both CMIP5 groups are strongly related to the mean states of precipitation in the models. For example, the group 2 with more severe “double-ITCZs” (“dry equator”) in its precipitation climatology than the group 1 also shows more obvious bias of the double positive anomaly bands over the eastern Pacific (near zero equatorial anomaly band in the Pacific Ocean) in its ENSO-related precipitation.

Comparing the ENSO-related precipitation in the CMIP5 models with the REC and the 20CR, most of the CMIP5 models also tend to simulate more positive anomalies over the western tropical Pacific and Indian Ocean, and the more negative ones over the southeastern Indian Ocean and SPCZ region. And group 2 models highly agree on the bias of near zero equatorial anomalies over the Pacific Ocean. The model agreement on the same sign shared by the precipitation climatology biases and the ENSO-related precipitation anomaly ones (Fig. 10) indicates that the ENSO-related precipitation biases of near zero equatorial anomalies and larger anomalies over the Maritime Continent and the western Indian Ocean are strongly connected with the overestimated/underestimated precipitation mean states over these regions. One possible explanation for the connection between near zero equatorial anomalies and “dry equator” bias is that the models with wide “dry equator” in their precipitation climatology may not be able to close the gap between the SPCZ and the ITCZ during El Niño when these two convergence zones merge together, thus leaving obvious near zero anomaly bands in their ENSO-related precipitation patterns. Another bias of the ENSO-related precipitation, the eastern Pacific double positive anomaly bands, may be associated with the well-known “double-ITCZs” precipitation bias in the precipitation mean state, especially over the Southern Hemisphere. This connection between these two biases is more obvious in the REC than the 20CR as shown in the maps of model agreement on same sign shared by precipitation climatology biases and El Niño-related ones (Fig. 10), indicating that this connection is sensitive to the choice of the

observational reference. The SVD results suggest that the double positive anomaly bands bias is also related with the models' ENSO-related SST biases in the eastern tropical Pacific Ocean.

Overall, in comparisons with the REC and the 20CR, the CMIP5 models show their ability to simulate the precipitation climatology and ENSO-related precipitation features that are similar to the observations. One goal of this paper is to provide information about the regions of the spatial patterns that need to be improved. We explain some of the spatial disagreements between the models and the observations ENSO-related precipitation by using the biases of precipitation mean states and SVD ENSO-related SST. The precipitation mean state and ENSO SST can exert great influences on the ENSO-related precipitation in the models; meanwhile, ENSO can also affect the precipitation mean state and result in changes in the air-sea interaction. In addition, the biases of other ENSO-related parameters such as zonal wind stress and diabatic heating can play roles in causing the ENSO-related precipitation biases in the models (Zhang and Jin 2012; Ham and Kug 2014). Therefore, more studies are needed in the future in order to significantly improve the ENSO-related precipitation in the general circulation models.

Acknowledgments We acknowledge the World Climate Research Programme's Working Group on Coupled Modeling, which is responsible for CMIP5 models. We also acknowledge 20CR V2 data provided by the NOAA/OAR/ESRL PSD, Boulder, Colorado, USA, from their website at http://www.esrl.noaa.gov/psd/data/gridded/data.20thC_ReanV2.html as well as the reconstructed precipitation dataset provided by Dr. Tom Smith (NOAA). We also appreciate the research guidance from Dr. Sumant Nigam and the three anonymous reviewers for their helpful comments/suggestions. This work is supported by the NOAA Cooperative Institute for Climate and Satellite, with Award Number NA09NES4400006.

References

- Adler RF et al (2003) The version-2 global precipitation climatology project (GPCP) monthly precipitation analysis (1979–present). *J Hydrometeorol* 4:1147–1167
- Bellenger H, Guilyardi E, Leloup J, Lengaigne M, Vialard J (2014) ENSO representation in climate models: from CMIP3 to CMIP5. *Clim Dyn* 42:1999–2018. doi:10.1007/s00382-013-1783-z
- Bellucci A, Gualdi S, Navarra A (2010) The double-ITCZ syndrome in coupled general circulation models: the role of large-scale vertical circulation regimes. *J Clim* 23:1127–1145. doi:10.1175/2009JCLI3002.1
- Bretherton CS, Smith C, Wallace JM (1992) An intercomparison of methods for finding coupled patterns in climate data. *J Clim* 5:541–560
- Bollasina MA, Ming Y, Ramaswamy V (2011) Anthropogenic aerosols and the weakening of the South Asian summer monsoon. *Science* 334(6055):502–505. doi:10.1126/science.1204994
- Brown JN, Sen Gupta A, Brown JR, Muir LC, Risbey JS, Whetton P, Wijffels SE (2013a) Implications of CMIP3 model biases and uncertainties for climate projections in the western tropical Pacific. *Clim Change* 119:147–161. doi:10.1007/s10584-012-0603-5
- Brown JR, Moise AF, Colman RA (2013b) The South Pacific convergence zone in CMIP5 simulations of historical and future climate. *Clim Dyn* 41:2179–2197. doi:10.1007/s00382-012-1591-x
- Brown JN, Langlais C, Maes C (2014) Zonal structure and variability of the Western Pacific dynamic warm pool edge in CMIP5. *Clim Dyn* 42:3061–3076. doi:10.1007/s00382-013-1931-5
- Chikira M, Sugiyama M (2010) A cumulus parameterization with state-dependent entrainment rate. Part I: description and sensitivity to temperature and humidity profiles. *J Atmos Sci* 67:2171–2193. doi:10.1175/2010JAS3316.1
- Clarke A (2008) An introduction to the dynamics of El Niño and the Southern Oscillation. Academic Press, Waltham, p 324
- Compo GP, Whitaker JS, Sardeshmukh PD, Matsui N, Allan RJ, Yin X, Worley SJ (2011) The twentieth century reanalysis project. *Q J R Meteorol Soc* 137(January):1–28. doi:10.1002/qj.776
- Curtis S, Adler R (2000) ENSO indices based on patterns of satellite-derived precipitation. *J Clim* 13:2786–2793. doi:10.1175/1520-0442(2000)013<2786:EIBOPO>2.0.CO;2
- Dai A, Wigley TML (2000) Global patterns of ENSO-induced precipitation. *Geophys Res Lett* 27(9):1283–1286. doi:10.1029/1999GL011140
- De Szoek SP, Xie SP (2008) The tropical eastern pacific seasonal cycle: assessment of errors and mechanisms in IPCC AR4 coupled ocean-atmosphere general circulation models. *J Clim* 21:2573–2590. doi:10.1175/2007JCLI1975.1
- Große MR, Brown JN, Narsey S, Brown JR, Murphy BF, Langlais C, Irving DB (2014) Assessment of the CMIP5 global climate model simulations of the western tropical Pacific climate system and comparison to CMIP3. *Int J Climatol* 3399(February):3382–3399. doi:10.1002/joc.3916
- Guilyardi E, Wittenberg A, Fedorov A, Collins M, Wang C, Capotondi A, Stockdale T (2009) Understanding El Niño in ocean-atmosphere general circulation models: progress and challenges. *Bull Am Meteorol Soc* 90(March):325–340. doi:10.1175/2008BAMS2387.1
- Ham Y-G, Kug J-S (2014) ENSO phase-locking to the boreal winter in CMIP3 and CMIP5 models. *Clim Dyn* 43:305–318. doi:10.1007/s00382-014-2064-1
- Ham Y-G, Kug J-S (2015) Improvement of ENSO simulation based on intermodel diversity. *J Clim* 28:998–1015. doi:10.1175/JCLI-D-14-00376.1
- Hirota N, Takayabu YN (2013) Reproducibility of precipitation distribution over the tropical oceans in CMIP5 multi-climate models compared to CMIP3. *Clim Dyn* 41:2909–2920. doi:10.1007/s00382-013-1839-0
- Huffman GJ, Adler RF, Bolvin DT, Gu G, Nelkin EJ, Bowman KP, Hong Y, Stocker EF, Wolff DB (2007) The TRMM multi-satellite precipitation analysis: quasi-global, multi-year, combined-sensor precipitation estimates at fine scale. *J Hydrometeorol* 8:38–55
- Huffman GJ, Adler RF, Bolvin DT, Gu G (2009) Improving the global precipitation record: GPCP version 2.1. *Geophys Res Lett* 36:L17808. doi:10.1029/2009GL040000
- Hwang YT, Frierson DMW, Kang SM (2013) Anthropogenic sulfate aerosol and the southward shift of tropical precipitation in the late 20th century. *Geophys Res Lett* 40(April):2845–2850. doi:10.1002/grl.50502
- Kim ST, Cai W, Jin FF, Yu JY (2014) ENSO stability in coupled climate models and its association with mean state. *Clim Dyn* 42:3313–3321. doi:10.1007/s00382-013-1833-6
- Kirtman BP, Fan Y, Schneider EK (2002) The COLA global coupled and anomaly coupled ocean–atmosphere GCM. *J Clim* 15:2301–2320. doi:10.1175/1520-0442(2002)015,2301:TCGCAA.2.0.CO;2
- Kug JS, Jin FF, An S-I (2009) Two types of El Niño events: cold tongue El Niño and warm pool El Niño. *J Clim* 22:1499–1515. doi:10.1175/2008JCLI2624.1

- Larkin NK, Harrison DE (2005) Global seasonal temperature and precipitation anomalies during El Niño autumn and winter. *Geophys Res Lett* 32:L16705. doi:[10.1029/2005GL022860](https://doi.org/10.1029/2005GL022860)
- Lin JL (2007) The double-ITCZ problem in IPCC AR4 coupled GCMs: ocean-atmosphere feedback analysis. *J Clim* 20:4497–4525. doi:[10.1175/JCLI4272.1](https://doi.org/10.1175/JCLI4272.1)
- Lindzen RS, Nigam S (1987) On the role of sea surface temperature gradients in forcing low-level winds and convergence in the tropics. *J Atmos Sci*. doi:[10.1175/1520-0469\(1987\)044<2418:OTROSS>2.0.CO;2](https://doi.org/10.1175/1520-0469(1987)044<2418:OTROSS>2.0.CO;2)
- McPhaden MJ, Zebiak SE, Glantz MH (2006) ENSO as an integrating concept in earth science. *Science* 314(December):1740–1745. doi:[10.1126/science.1132588](https://doi.org/10.1126/science.1132588)
- Mechoso CR, Robertson AW, Barth N, Davey MK, Delecluse P, Gent PR, Tribbia JJ (1995) The seasonal cycle over the tropical pacific in coupled ocean–atmosphere general circulation models. *Mon Weather Rev*. doi:[10.1175/1520-0493\(1995\)123<2825:TSCOTT>2.0.CO;2](https://doi.org/10.1175/1520-0493(1995)123<2825:TSCOTT>2.0.CO;2)
- Meehl GA (1987) The annual cycle and interannual variability in the tropical Pacific and Indian Ocean regions. *Mon Weather Rev*. doi:[10.1175/1520-0493\(1987\)115<0027:TACAIV>2.0.CO;2](https://doi.org/10.1175/1520-0493(1987)115<0027:TACAIV>2.0.CO;2)
- Nigam S, Chung C, DeWeaver E (2000) ENSO diabatic heating in ECMWF and NCEP reanalyses, and NCAR CCM3 simulation. *J Clim* 13:3152–3171
- Philander SGH (1985) El Niño and La Niña. *J Atmos Sci* 42:652–662
- Räsänen J (2007) How reliable are climate models? *Tellus, Ser A Dyn Meteorol Oceanogr* 59:2–29. doi:[10.1111/j.1600-0870.2006.00211.x](https://doi.org/10.1111/j.1600-0870.2006.00211.x)
- Rasmusson EM, Carpenter TH (1982) Variations in tropical sea surface temperature and surface wind fields associated with the Southern Oscillation/El Niño. *Mon Weather Rev*. doi:[10.1175/1520-0493\(1982\)110<0354:VITSST>2.0.CO;2](https://doi.org/10.1175/1520-0493(1982)110<0354:VITSST>2.0.CO;2)
- Rayner NA, Parker DE, Horton EB, Folland CK, Alexander LV, Rowell DP, Kaplan A (2003) Global analyses of sea surface temperature, sea ice, and night marine air temperature since the late Nineteenth Century. *J Geophys Res Atmos*. doi:[10.1029/2002JD002670](https://doi.org/10.1029/2002JD002670)
- Reichler T, Kim J (2008) How well do coupled models simulate today's climate? *Bull Am Meteorol Soc* 89:303–311. doi:[10.1175/BAMS-89-3-303](https://doi.org/10.1175/BAMS-89-3-303)
- Ropelewski CF, Halpert MS (1987) Global and regional scale precipitation patterns associated with the El Niño/Southern Oscillation. *Mon Weather Rev* 115:1606–1626. doi:[10.1175/15200493\(1987\)115<1606:GARSPP>2.0.CO;2](https://doi.org/10.1175/15200493(1987)115<1606:GARSPP>2.0.CO;2)
- Smith TM, Reynolds RW, Peterson TC, Lawrimore J (2008) Improvements to NOAA's historical merged land-ocean surface temperature analysis (1880–2006). *J Clim* 21:2283–2296. doi:[10.1175/2007JCLI2100.1](https://doi.org/10.1175/2007JCLI2100.1)
- Smith TM, Arkin PA, Ren L, Shen SSP (2012) Improved reconstruction of global precipitation since 1900. *J Atmos Ocean Technol* 29:1505–1517. doi:[10.1175/JTECH-D-12-00001.1](https://doi.org/10.1175/JTECH-D-12-00001.1)
- Sun D-Z, Zhang T, Sun Y, Yu Y (2014) Rectification of El Niño–Southern Oscillation into climate anomalies of decadal and longer time-scales: results from forced ocean GCM experiments. *J Clim* 27:2545–2561
- Taylor KE, Stouffer RJ, Meehl GA (2012) An overview of CMIP5 and the experiment design. *Bull Am Meteorol Soc* 93(april):485–498. doi:[10.1175/BAMS-D-11-00094.1](https://doi.org/10.1175/BAMS-D-11-00094.1)
- Trenberth KE (1976) Spatial and temporal variations of the Southern Oscillation. *Q J R Meteorol Soc* 102:639–653. doi:[10.1002/qj.49710243310](https://doi.org/10.1002/qj.49710243310)
- Trenberth KE, Caron JM (2000) The southern oscillation revisited: Sea level pressures, surface temperatures, and precipitation. *J Clim* 13(24):4358–4365. doi:[10.1175/1520-0442\(2000\)013<4358:TSORSL>2.0.CO;2](https://doi.org/10.1175/1520-0442(2000)013<4358:TSORSL>2.0.CO;2)
- Vincent DG (1994) The South Pacific convergence zone (SPCZ): a review. *Mon Weather Rev*. doi:[10.1175/1520-0493\(1994\)122<1949:TSPCZA>2.0.CO;2](https://doi.org/10.1175/1520-0493(1994)122<1949:TSPCZA>2.0.CO;2)
- Vincent EM, Lengaigne M, Menkes CE, Jourdain NC, Marchesio P, Madec G (2011) Interannual variability of the South Pacific convergence zone and implications for tropical cyclone genesis. *Clim Dyn* 36:1881–1896. doi:[10.1007/s00382-009-0716-3](https://doi.org/10.1007/s00382-009-0716-3)
- Wang C, Xie S-P, Carton JA (2004) A global survey of ocean–atmosphere interaction and climate variability. *Earth Clim Ocean Atmos Interact* 147:1–19. doi:[10.1029/147GM01](https://doi.org/10.1029/147GM01)
- Watanabe M et al (2010) Improved climate simulation by MIROC5: mean states, variability, and climate sensitivity. *J Clim* 23:6312–6335. doi:[10.1175/2010JCLI3679.1](https://doi.org/10.1175/2010JCLI3679.1)
- Whitaker JS, Hamill T (2002) Ensemble data assimilation without perturbed observations. *Mon Weather Rev* 130:1913–1924. doi:[10.1175/1520-0493\(2002\)130<1913:EDAWPO>2.0.CO;2](https://doi.org/10.1175/1520-0493(2002)130<1913:EDAWPO>2.0.CO;2)
- Widlansky MJ, Timmermann A, Stein K, McGregor S, Schneider N, England MH, Cai W (2012) Changes in South Pacific rainfall bands in a warming climate. *Nat Clim Change* 3(4):417–423. doi:[10.1038/nclimate1726](https://doi.org/10.1038/nclimate1726)
- Wittenberg AT, Rosati A, Lau NC, Ploshay JJ (2006) GFDL's CM2 global coupled climate models. Part III: tropical Pacific climate and ENSO. *J Clim* 19:698–722. doi:[10.1175/JCLI3631.1](https://doi.org/10.1175/JCLI3631.1)
- Wolter K, Timlin MS (1998) Measuring the strength of ENSO events—how does 1997/98 rank? *Weather* 53:315–324
- Xie P, Arkin P (1997) Global precipitation: a 17-year monthly analysis based on gauge observations, satellite estimates, and numerical model outputs. *Bull Am Meteorol Soc* 78:2539–2558. doi:[10.1175/1520-0477\(1997\)078<2539:GPAYMA>2.0.CO;2](https://doi.org/10.1175/1520-0477(1997)078<2539:GPAYMA>2.0.CO;2)
- Yeh SW, Kug JS, An SI (2014) Recent progress on Two types of El Niño: observations, dynamics and future changes. *Asia-Pac J Atmos Sci* 50(1):69–81. doi:[10.1007/s13143-014-0028-3](https://doi.org/10.1007/s13143-014-0028-3)
- Zhang C (2001) Double ITCZs. *J Geophys Res* 106(D11):11785–11792. doi:[10.1029/2001JD900046](https://doi.org/10.1029/2001JD900046)
- Zhang W, Jin FF (2012) Improvements in the CMIP5 simulations of ENSO-SSTA meridional width. *Geophys Res Lett* 39:L23704. doi:[10.1029/2012GL053588](https://doi.org/10.1029/2012GL053588)
- Zhang T, Sun DZ (2014) ENSO asymmetry in CMIP5 models. *J Clim* 27:4070–4093. doi:[10.1175/JCLI-D-13-00454.1](https://doi.org/10.1175/JCLI-D-13-00454.1)